PAUL SCHERRER INSTITUT

PSI

SwissFEL Experimental Station B: Conceptual design Report

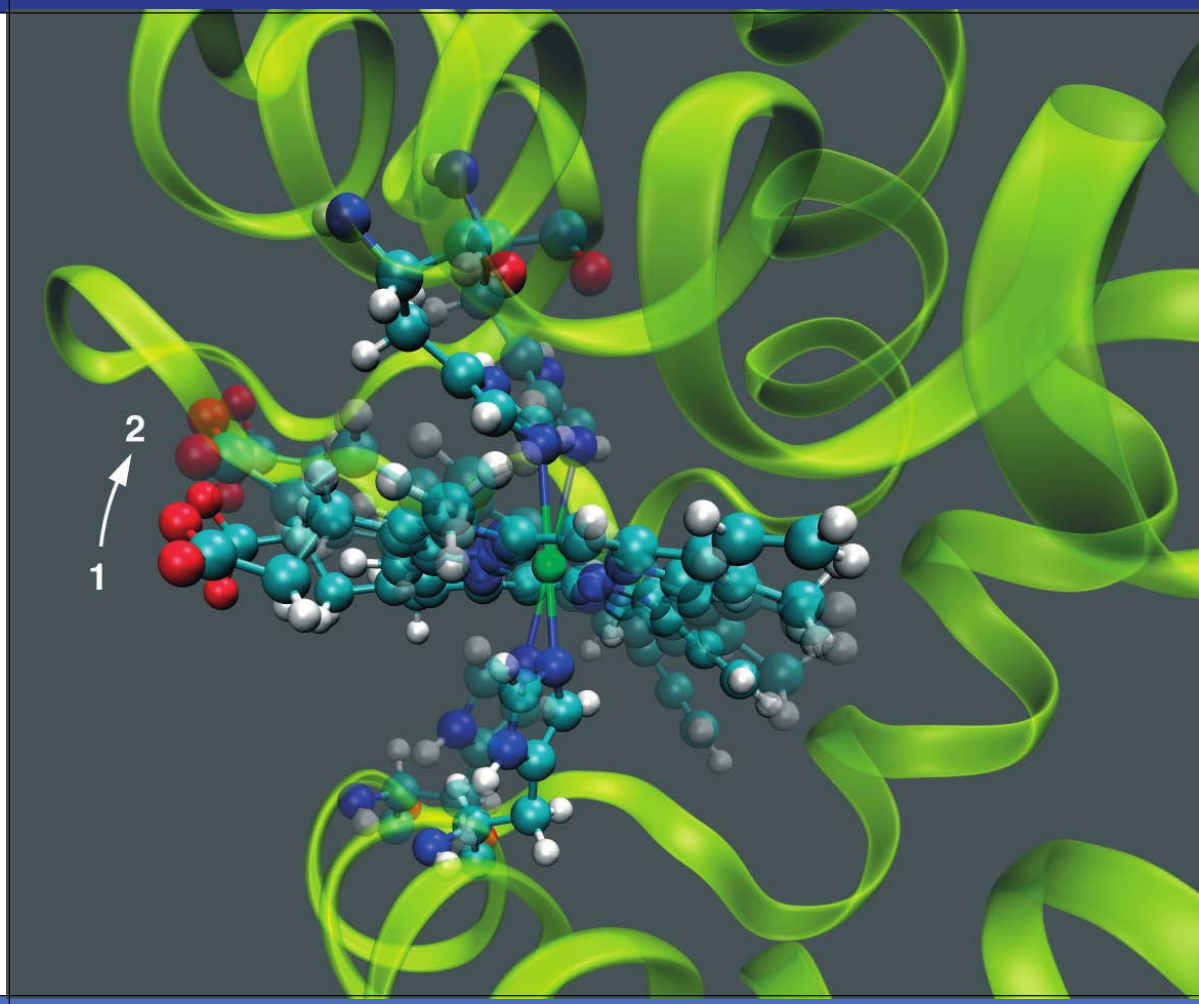

Status: June 2013

Conceptual Design Report
SwissFEL ARAMIS Endstation ES-B

Femtosecond X-Ray Pump-Probe Diffraction and Scattering Electronic and Magnetic Ordered Crystalline Materials

Gerhard Ingold and Paul Beaud

SwissFEL, Paul Scherrer Institute, CH-5232 Villigen - PSI

June 20, 2013

Contents

Summary

The proposed instrument combines time-resolved laser spectroscopy methods and X-ray scattering techniques to study the dynamics of cooperative interactions in crystalline materials that exhibit long-range electronic and magnetic order. Such materials also show complex phase diagrams. A important class are strongly correlated electron systems or 'quantum materials' that exhibit competition between lattice, charge, orbital and spin degrees of freedom. As a result new phases or states of condensed matter emerge from these correlations of the atomic, electronic and magnetic constituents. Recent examples include high temperature superconductivity, colossal magnetoresistance, metal-to-insulator transition, electron fractionalization and novel quantum-critical states. Multiferroics, materials combining several functional properties, hold promise for future device applications. To characterize and control such systems - especially when the system no longer is in strict thermodynamic equilibrium - is ideally done in the time domain where the coupled excitations can be distinguished on account of their different response and relaxation times.

Photon-in/photon-out scattering allows to directly correlate the electronic, magnetic and structural dynamics. At the hard X-ray ARAMIS beamline we propose to install an instrument for X-ray pump-probe scattering and diffraction including polarization control and flexible sample environment. It includes a fs laser system, the X-ray optics, the diagnostics and three experimental setups. In phase-I, (1) a general purpose heavy load sample stage with robot detector arm and cryo XPP chamber and (2) a heavy load diffractometer with detector arm including polarization analysis for elastic scattering tr(R)XRD at high magnetic fields. In phase-II, (3) a compact medium energy resolution spectrometer for inelastic scattering tr(R)IXS at high pressure, when ARAMIS self-seeding becomes available.

Chapter 1

Photon-in / Photon-out

All-optical time-resolved experiments on the femtosecond timescale using lasers are well established. This is not the case for X-rays. Employing X-rays in such experiments is a new field that still develops. With the advent of XFELS, the X-ray pump-probe (XPP) technique has become a new tool to study stimulated ultrafast dynamics in condensed matter. In this document we propose to construct a dedicated XPP instrument at the ARAMIS hard X-ray beamline of SwissFEL [1] to study femtosecond phenomena mainly in crystalline materials that exhibit long-range electronic and magnetization order. A important class are strongly correlated electron systems (recently also called 'quantum materials'). On a femtosecond timecale such materials are also studied by other methods which are new, namely time-resolved ARPES [2, 3], multi-THz spectroscopy[4], and electron diffraction [5]. We do not discuss these methods in more detail but focus on X-ray methods such as X-ray diffraction and resonant elastic and inelastic X-ray scattering which for static measurements are well established methods for the study of strongly correlated electron systems at exisiting X-ray synchrotron facilities.

To experimentally study an interacting electron system in condensed matter requires methods to identify low-energy quasiparticles (fermions) and their collective (bosonic) excitations. The measured quantity must allow to infer information about the spectroscopic properties of quasiparticle excitations, about the dynamic properties of bosonic collective modes, and about the electronic correlations embedded in the two-particle properties of the Hamiltonian in case of strongly correlated electron systems. Such information can be inferred from the dynamic structure factor $S(\tilde{q}, \omega)$ which is measured in X-ray scattering. X-ray scattering is a photon-in / photon-out technique which offers important advantages:

- In principle, the energy-, momentum- and polarization change of the scattered photon (which is transferred to intrinsic excitations of the system) is measured.
- X-rays strongly couple to charge and orbital degrees of freedom and can be sensitive to magnetization.
- Resonant enhancement of electronic signals (sometimes by several orders of magnitude) by tuning the incident X-ray energy to characteristic absorption edges of the material.
- Different aspects of the excitation can be probed by exploiting selection rules for both the pump and probe beam.
- Resonant and non-resonant X-ray diffraction (coherent elastic scattering) can measure long-range atomic, electronic and magnetic order.
- Resonant and non-resonant inelatic X-ray scattering can measure lattice, electronic and magnetic (spin) modes with momentum resolution and hence the respective dispersion relations.

- Elastic and inelastic X-ray scattering are sensitve to both thermal and non-thermal (quantum mechanical) fluctuations.
- The characteristic X-ray energy and polarizaton dependence by tuning to resonances offer elemental-, chemical- and bonding specificity.
- The expected energy scale for bosonic excitations in strongly correlated electron systems in the range 1 - 100 meV can be covered.
- More flexible sample environments beyond high pressure, including high magnetic or electric fields.
- The study of non-equilibrium dynamics with pump-probe techniques.

In a X-ray scattering experiment the fraction of photons of incident energy E scattered into a solid angle $\mathrm{d}\Omega$ with an energy between E' and $\mathrm{E}' + \mathrm{dE}'$ is given by the partial double differential cross section. For charge scattering from N charges the non-resonant (non-relativistic) X-ray cross section is given by [6]

$$\frac{\mathrm{d}^2\sigma}{\mathrm{d}\Omega \mathrm{dE}'} = N\, r_e^2\, \frac{k'}{k}\, \{\vec{\epsilon}\cdot\vec{\epsilon}\,'\}^2\, \mathrm{S}(\vec{q},\omega)$$

and

$$S(\vec{q},\omega) = \frac{1}{2\pi\hbar N}\int_{-\infty}^{+\infty} \mathrm{dt}\; e^{-i\omega t}\; \langle \mathrm{n}^+(\vec{q})\, \mathrm{n}(\vec{q},t)\rangle$$

where the dynamic structure factor $S(\vec{q},\omega)$ is the time Fourier transform of the charge fluctuation spectrum described by the correlation function $\langle \mathrm{n}^+(\vec{q})\, \mathrm{n}(\vec{q},t)\rangle$ (in information theory this relation is also known as Wiener-Khinchin theorem). Similarly for magnetic scattering the dynamic structure factor is expressed by the correlation function $\langle \mu^+(\vec{q})\, \mu(\vec{q},t)\rangle$. The time dependence are given by the Heisenberg operators $\mathrm{n}(\vec{q},t)$ and $\mu(\vec{q},t)$). The momentum transfer of the scattering process is represented by $\vec{q} = \vec{k}' - \vec{k} (E = \hbar c k, E' = \hbar c k')$, the energy transfer by $\omega = (\mathrm{E} - \mathrm{E}')/\hbar$, respectively. The polarization dependence is described by the term $\{\vec{\epsilon}\cdot\vec{\epsilon}\,'\}$ and ϵ and ϵ' are, respectively, the polarization vector of the incoming and scattered photon. By definition, $\vec{\epsilon}\cdot\vec{k} = \vec{\epsilon}\,'\cdot\vec{k} = 0$.

The strictly elastic component ($\omega \to 0$) of the response function is derived from the infinite-time limit of the correlation function where $\langle n^+(\vec{q})\, n(\vec{q}, t=\infty)\rangle = |\langle n(\vec{q})\rangle|^2$. Hence for elastic scattering we have

$$\left(\frac{\mathrm{d}^2\sigma}{\mathrm{d}\Omega}\right)_{el} = r_e^2\, \{\vec{\epsilon}\cdot\vec{\epsilon}\,'\}^2\; \delta(\hbar\omega)\; |\langle n(\vec{q})\rangle|^2$$

and

$$S(\vec{q},\omega\to 0) = \frac{1}{N}\, \delta(\hbar\omega)\; |\langle n(\vec{q})\rangle|^2$$

where the delta function is expressed as $\delta(\hbar\omega) = (2\pi)^{-1}\; \int \mathrm{dt}\; e^{i\omega t}$. The quantity $\langle n(\vec{q})\rangle$ ($\langle \mu(\vec{q})\rangle$) is the thermal average of the Fourier transform of the charge density $\rho(\vec{r})$ (magnetization density $\mathrm{m}(\vec{r})$) since $\mathrm{n}(\vec{q}) = \sum_j e^{i\vec{q}\vec{r}_j} = \int \mathrm{d}\vec{r}\, \rho(\vec{r})\, e^{i\vec{q}\vec{r}}$ where $\vec{r_j}$ is the position of the charge labelled by index j.When averaged with respect to all other parameters required to describe the target assembly, the elastic cross section includes both coherent elastic scattering (Bragg diffraction) $(\mathrm{d}^2\sigma/\mathrm{d}\Omega)_{el,ch} \propto |\,\overline{\langle \mathrm{n}_{ch}(\vec{q})\rangle}\,|^2$ and incoherent elastic (diffuse) scattering $(\mathrm{d}^2\sigma/\mathrm{d}\Omega)_{el,ich} \propto |\,\overline{\langle n_{ich}(\vec{q})\rangle}\,|^2$.

Under the assumption that the charge density is localized at the positions of the basis atoms of the unit cell, in the case of Bragg diffraction from a crystal we have $\overline{F}_{hkl} = |\,\overline{\langle \mathrm{n}_{ch}(\vec{q})\rangle}\,|^2$ where the intensity of a Bragg reflection hkl given by the structure factor

$$F_{hkl} \;=\; \sum_j f_j\, e^{i\vec{q}\,\vec{r}_j}\; e^{-\frac{1}{2}\,\langle(\vec{u}_j\;\vec{q})^2\rangle}$$

depends on the atomic form factor f_j and the relative position $\vec{r}_j$ of the j^{th} basis atom in the crystal unit cell. The Debye Waller (DWF) $e^{-1/2\langle(\vec{u}_j\,\vec{q})^2\rangle}$ expresses the decrease in F_{hkl} due to incoherent displacements $\vec{u}_j$ of the atoms. Momentum conservation requires $\vec{q} = \vec{G}$ where the crystal momentum is given by the reciprocal-lattice vector $\vec{G}$.

The power of X-rays in the study of electronic excitations is partly derived from the direct relationship between the cross section and the complex dielectric function $D(\vec{q},\omega)$

$$S(\vec{q},\omega) \propto \frac{\hbar}{2\pi e^2}\,\vec{q}^2\,\mathrm{Im}\left[D^{-1}(\vec{q},\omega)\right]$$

This is the charge scattering version of the dissipation-fluctuation theorem. A similar relation holds for magnetic scattering and the complex magnetic susceptibility $\chi(\vec{q},\omega)$. Both $D(\vec{q},\omega)$ and $\chi(\vec{q},\omega)$ can be viewed as a bulk response function similar to the specific heat which (at constant pressure) is proportional to the mean-square fluctuations in the entropy. The 'dielectric response function' and, respectively, the 'magnetic susceptibility response' are proportional to frequency and wave-vector-dependent fluctuations in the total charge and magnetization density. When the dissipation-fluctuation relation is valid, $D(\vec{q},\omega)$ and $\chi(\vec{q},\omega)$ can be determined from $S(\vec{q},\omega)$ and compared to theoretical model calculations.

To study the time-dependent response to an external perturbation, real time correlation functions of observable operators are appropriate because they naturally relate to experimental probes such as the dynamic structure factor $S(\vec{q},\omega)$, the quantity which is measured in a scattering experiment:

- Remarkably, the response $S(\vec{q},\omega)$ of a material depends on its fluctuations. This is valid even for quantum fluctuations at zero temperature [7].
- Correlation functions are usually complex quantities, the imaginary part coming from quantum aspects (it vanishes for $\hbar \to 0$).
- Detailed balance $S(\vec{q},\omega) = e^{-\hbar\omega/\mathrm{k}_B T}\,S(-\vec{q},-\omega)$ is valid because $S(\vec{q},\omega)$ is a response function and therefore purely real. [Note: the condition of detailed balance may not be valid under nonequilibrium conditions.]
- A imaginary or negative response function is a signature of a material that is unstable with respect to induced perturbations (fluctuations).
- The relation for $S(\vec{q},\omega)$ is derived using Fermi's Golden Rule for transition rates and hence on first-order perturbation theory (i.e. it describes the linear response of the material and must be extended for non-linear X-ray studies).

For understanding the statistical behaviour of a (quantum mechanical) system under nonequilibrium conditions it is not clear if a framework similar to the Boltzmann-Gibbs does exist, for example under nonequilibrium conditions the fluctuation- dissipation theorem does not hold in general and we should consider response functions separately from the correlations.

One approach to finding such a formalism from microscopic laws is to understand how a system responds to perturbations when it is driven out of equilibrium and how subsequently local or collective and long-range fluctuations evolve. The time dependence will be encoded in the correlation functions and hence in the frequency response given by the time Fourier transform, as shown by two illustrative examples:

- for a pure exponential decay $\propto e^{-\Gamma t}$ of the correlation function the lineshape of the response function (i.e. dynamic structure factor) will be a Lorentzian

  $$S(\vec{q},\omega) \propto \frac{\Gamma}{(\omega^2+\Gamma^2)}$$

  with width Γ.

- for an oscillatory decaying correlation function $\propto \exp(-\Gamma t)\cos(\omega_0 t)$ the lineshape of the response function exhibits two Lorentzians

$$S(\vec{q},\omega) \propto \frac{\Gamma}{\pi}\frac{\Gamma^2+\omega^2+\omega_0^2}{(\Gamma^2+(\omega-\omega_0)^2)\,(\Gamma^2+(\omega-\omega_0)^2)}$$

  with two peaks at $\omega = \pm\sqrt{\omega_0^2-\Gamma^2}$.

The full statistics of the fluctuations (i.e. the standard deviation, their asymmetry, and so on) is measured by the statistical moments of $S(\vec{q},\omega)$. These moments reflect the statistics of the current associated with the motion of energy carriers or caused by the perturbations. In a generalized Boltzmann-Gibbs framework this current could be the equivalent to the free energy. Hence knowing the full current statistics is practically equivalent to knowing the 'generating function' from which all higher order correlation functions, all possible states of the system and their corresponding statistical weight can be calculated. This way dynamic nonequilibrium experiments could be compared to quantum statistical theories at any spatiotemporal scale.

The dynamic structure factor (and hence the cross section) describes the response of the system and is the time Fourier transform of a correlation function which describes charge and, respectively, magnetization fluctuations probed by charge and magnetic scattering. Non-resonant magnetic X-ray scattering is very weak. [Note that the correlation function is the same as that measured by inelastic neutron scattering, except in the latter case it is the nuclear and magnetic densities that are probed.] In a time-resolved scattering experiment the double differential cross section which describes the fraction of scattered X-rays is measured as a function of pump-probe delay. The X-ray scattering techniques employed at ARAMIS ES-B are summarized in Table 1.1.

Time-Resolved Photon-In / Photon-Out Experiments	
Probing changes of lattice order and symmetry	
time-resolved (Bragg) X-ray diffraction	**trXRD**
Probing electronic and magnetic order and their symmetry	
time-resolved resonant elastic X-ray diffraction	**trRXRD**
time-resolved resonant inelastic X-ray scattering	**trRIXS**
time-resolved X-ray magnetic dichroism	**trXMCD**
Probing non-linear changes of the susceptibility	
time-resolved non-linear X-ray scattering (spectroscopy)	**trNLXS**
Probing dynamical fluctuations (atomic, electronic and magnetic)	
time-resolved thermal diffuse scattering	**trTDS**
time-resolved non-thermal diffuse scattering	**trNTDS**

Table 1.1: X-ray methods proposed for pump-probe experiments at ES-B.

Time-resolved elastic scattering measures the change of the static structure factor $S(\vec{q},\omega=0)$ which includes contributions from Bragg diffraction (trXRD, coherent elastic scattering) which measures a change of lattice constants of the static long-range order and high resolution minute changes in the lattice symmetry. The ordered state is characterized by the static (phase) coherence length ξ_S. TrXRD probes the change of long-range order and at grazing incidence can measure the atomic dynamics in the bulk, at surfaces and interfaces of crystalline environment. Time-resolved diffuse scattering probes fluctuations of thermally (trTDS) or quantum-mechanically (non-thermally, trNTDS) activated dynamic modes induced by the pump beam. The diffuse scattering is characterized by the fluctuating correlation length ξ_F.

The atomic structure dynamics will be related to electronic (charge and orbital) and magnetic (spin) strucure dynamics by employing time-resolved resonant X-ray diffraction

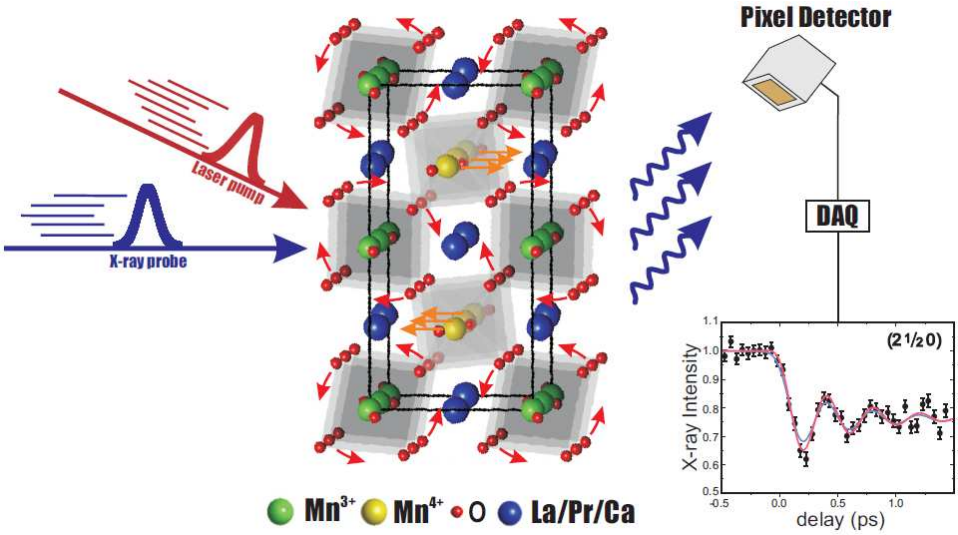

Figure 1.1: **Schematic of a X-ray pump-probe (XPP) scattering experiment.** A laser- or THz-pump-pulse excites a crystalline material, for example a CMR manganite, which exhibits long-range lattice-, charge-, orbital- and spin-order. The response of the material is measured by photon-in/photon-out scattering of a X-ray probe-pulse focussed onto the same spot. Before reaching the sample, the pump pulse bounces of a movable mirror pair (not shown) that provides a time delay between the excitation of the pump and the arrival of the probe. A 2D pixel detector records the transient, pump-induced fractional change in scattered intensity ΔI (normalized to the incoming X-ray intensity I_0) as a function of the time delay from the moment of pump excitation. A data acquisisition (DAQ) reads out the detector shot-by-shot and writes the data onto disk. In our example, the time trace of a coherent optical phonon is recorded by measuring the change of the diffracted X-ray intensity of the structural (2 1/2 0) superlattice reflection in LPCMO manganite which is coupled to charge and orbital order [24]. The red arrows indicate the motion of the atoms induced by the laser pump-pulse. Similarly the dynamics of the electronic and spin order can be measured with resonant scattering. The scheme shown here can be extended in several ways, namely by employing polarized beams, by tuning the material by an external parameter (temperature, pressure or magnetic field), or by installing a spectrometer between the sample and the detector to disperse inelastically scattered X-rays in the case of tr(R)IXS.

(trRXRD) and time-resolved X-ray magnetic dichroism (trXMCD). The dynamics of the non-linear response of the material - the non-linear change of the susceptibility - is measured by time-resolved non-linear X-rays scattering (trNLXS).

Time-resolved inelastic X-ray scattering (trIXS) measures the full dynamic structure factor $S(\vec{q},\omega)$ and can directly probe ξ_F. It describes the response in terms of a quasiparticle excitation that propagates through the material carrying momentum $\hbar\vec{q}$ andenergy $\hbar\omega$. In case of inelastic X-ray scattering (RIXS) the quasiparticle excitation is a valence band excitation that can couple to the charge or magnetization density. Time-resolved RIXS (trRIXS) can examine the temporal evolution of the dispersion relation of quasiparticle excitations and elementary orbital and spin excitations.

1.1 Pump-probe

In a X-ray pump-probe (XPP) experiment the fractional change of the (normalized) intensity $\Delta I/I_0$ of the scattered X-ray probe-pulse is measured as a function of time between the arrival of the pump and the arrival of the probe on the sample. Figure 1.1 illustrates the basic version of a XPP experiment which can be extended in several ways. For the purpose of this paper we note:

- For the majority of experiments considered here we assume that the pump- and probe-excitation of the system proceeds in two steps which are independent of each other. This means the probe measures the response of the material when the pump no longer is present. Therefore standard X-ray methods as outlined above can be applied without taking non-linear X-ray processes (such as optical-X-ray mixing, etc.) into account. **Although non-linear X-ray experiments will be an interesting and important class of experiments, it is too early to say that it will establish a field in its own and will require instrumentation beyond what is proposed in this document.**

- We assume that single-shot experiments will be an exception and that almost all experiments will be done in a stroboscopic and repetitive manner. The main reason is that electronically or magnetically ordered crystalline materials are senstitive to radiation damage. Experiments so far have shown that a limit exists both for the pump and probe on the number of photons per pulse which is well below the single-shot ablation threshold. 'Refreshing sample' techniques could be a solution, but large and very homogeneous crystalline samples would be needed which are not available in most cases. We therefore assume that most experiments will be done stroboscopically. This requires that the system returns to its initial state after each shot. **Although single-shot experiments are not excluded, no extra instrumentation is proposed in this document beyond what is needed for stroboscopic measurements.**

- The level of fractional change that can be measured depends on the stability of the pump- and probe-pulse in intensity, energy (wavelength) and time (arrival time and pulse length). Thanks to the stability of Ti:sapphire laser systems, fractional changes in all-optical pump-probe measurements (in reflectivity or transmission) of less than one part in a million can be time resolved on a femtosecond time scale. For measurements at a SASE X-ray source, where all three quantities fluctuate, an ambitious goal would be an accuracy of one part in a thousand with time resolution 10 fs FWHM. To achieve this, advanced shot-to-shot X-ray diagnostic tools have to be implemented.

- To cover a broad range of systems, we propose to implement flexible pump and probe pulses in terms of tunable wavelength, variable focussing and intensity, and linear or circular polarization. In addition it should be possible that the material

can (statically) be tuned by an external parameter such as temperature, pressure, and magnetic or electric field. For example, far-IR (THz) pump-pulses are provided by optical rectification or UV pulses by harmonic generation. With a far-IR pulse experiments can selectively probe low-energy modes, such as the superconducting energy gap or specific lattice vibrations. **X-ray-pump and X-ray-probe experiments on the femtosecond time scale that require the installation of a X-ray split-and-delay unit based on thin crystals are not considered here.**

- The main focus of the scientific case presented in this document is to study the time dependent behaviour of correlated crystalline materials that exhibit long-range electronic and magnetization order. This type of experiments are the basis for the current R&D effort (see Appendix A), for the specifications and the outline of the instrumentation (see Section 3 and Appendix B). **However, this does not exclude pump-probe X-ray scattering on liquid molecular systems [8], on crystalline organic systems [9, 10] , on powders (Laue diffraction) [11], coherent diffraction imaging of nanocrystals [12], non-linear phononics [13], etc., as long as the instrumentation proposed in this document is sufficient to perform such experiments or new instrumentation not considered here is provided by the users**

Chapter 2

Scientific Case

The study of the time dependent behaviour of correlated materials in condensed matter may be divided into two broad classes, weakly correlated (which may be understood in terms of non-interacting particles in the framework of Landau-Fermi liquid theory) and strongly correlated (which cannot be understood from an independent particle perspective). The main focus are strongly correlated electron systems ('quantum materials') of long-range atomic-, charge-, orbital- and spin order that exhibit complex phase diagrams due to competing orders. Frequently in strongly correlated systems many of the energy scales are of similar size: Hubbard interaction (U$\sim$ 1-4 eV), hopping integral (t$\sim$ 0.5 eV), magnetic exchange (J$\sim$0.15 eV), charge-transfer energy ($\Delta \sim$ 2 eV), and Jahn-Teller splitting ($\Delta_{JT} \sim$1 eV). The ground state is obtained by minimizing the total energy. Ground states include: ferromagnetism (FM), antiferromagnetism (AFM), metals, insulators, semiconductors, ferroelectrics, superconductors, and others.

The fine balance of all the energy scales give rise to competing orders and small changes can lead to switching of states and to large changes in the properties. The ground state of the N-electron system in equilibrium (and in the thermodynamic limit $N \to \infty$) of a crystalline solid exhibiting electronic and magnetic order can be characterized by a combination of general properties such as:

- Charge ($\leftrightarrow$ insulator, metal, superconductor);
- Spin ($\leftrightarrow$ ferromagnet, antiferromagnet, paramagnet);
- Dimensionality ($\leftrightarrow$ 1D-chain, 2D-layer, 3D-lattice);
- Symmetry ($\leftrightarrow$ spatial, time, parity);
- Invariance ($\leftrightarrow$ translation, rotation, inversion);
- Scale ($\leftrightarrow$ local, non-local, global);
- Statistics ($\leftrightarrow$ fermion, boson);
- Superposition ($\leftrightarrow$ incoherent, coherent, entangled);
- Order ($\leftrightarrow$ lattice, charge, orbital, spin).

Strongly correlated systems then exhibit extreme sensitivity to pertubation including: temperature T, pressure P, magnetic fields B, electric fields E, doping, defects and photons. Upon stimulation with a photon, the system will change into an excited state (or different phase) and no longer will be in strict thermodynamic equilibrium. The dynamics of competing orders and interactions is encoded in the response of the system and reveals as coupled collective excitations, both coherent and incoherent. By measuring these excitations in real time and with atomic resolution at the intrinsic timescale of the underlying structural and electronic dynamics, the nature of the competing orders could be disentangled. For simplicity we divide its response in four areas:

1. Dynamics of collective modes:
   phonons, orbital waves, charge and spin density waves;

2. Dynamics and switching in (multi)ferroic materials:

elastic, electronic and magnetic (coupled) switching phenomena;

3. Non-equilibrium phase transitions at energy scale 0.1 - 5 eV (10^3 - 10^4 K);
   First order: strongly coupled systems exhibiting phase coexistence and latent heat;
   Second order: weakly coupled systems exhibiting fluctuations and correlations;

4. Non-equilibrium and equilibrium phase transitions at energy scale 10^{-3}-10^{-2} eV (10^1-10^2 K):
   weakly coupled systems close to a quantum critical point.

Phase transitions occur due to a competition between fluctuations and interactions. They are found at finite (zero) temperature in classical (quantum) phase transitions as some system parameter is varied, such as applied hydrostatic pressure, chemical doping, or applied magnetic field. Amongst the plethora of strongly correlated systems there are some hints of general underlying principles that guide the science into several overlapping directions:

- (Coherent) dynamics and coupling in nonequilibrium systems;
- Correlations and fluctuations in nonequilibrium phase transitions;
- Real-time evolution of electronic correlations;
- Selective excitation of electronic, spin and structural order;
- Coupling, control and switching in multiferroics;
- Non-linear transient response in condensed matter systems;
- (Quantum) control of response functions.

2.1 Time resolved X-ray diffraction (trXRD)

Away from an absorption edge, X-rays interact predominantly with tightly bound core level electrons, providing information about the relative positions of atoms. Spatially homogeneous structural 'fast dynamics' (timescale $\sim$ 0.01 - 10 ps) induced by the pump-beam result from time-dependent changes in the structure factor $S(\vec{q}, \omega = 0) \propto |F_{hkl}|^2$ due to the dependence on the basis-atom positions $\vec{r}_j$ (i.e. dynamics of the mean of the atomic positions, coherent optical phonons) and/or on the displacements $\vec{u}_j$ (i.e. dynamics of the variance of the atomic positions from the mean value, 'phonon squeezing'). The spatially inhomogeneous 'slow dynamics' (timescale $\sim$ 10 - 100 ps) show the onset of strain (from coherent acoustic phonons) and thermalization (incoherent optical and acoustic phonons), followed by thermal diffusion that drives the near-surface temperature of the sample back down to its original value.

2.1.1 Grazing incidence diffraction

In opaque solids, optical-wavelength photons are usually absorbed in a very thin surface layer ranging from 10 - 100 nm, whereas the attenuation length extends typically into the μm-scale for X-ray wavelengths near 1 Å. One way to avoid this undesirable mismatch of excited and probed sample volume is to use thin films. In cases where the X-ray scattering is weak (because of low flux and/or low diffraction efficiency), a more efficient solution is to apply a grazing-incidence, non-coplanar asymmetric diffraction geometry [14, 15]. In case of single crystals, this geometry allows one to match the absorption depth of the X-ray probe to the spatial excitation depth by setting the incidence angle of the X-rays to values near the critical angle for total external reflection. Our work on non-equilibrium phonon dynamics studied by grazing-incidence femtosecond X-ray crystallography has been summarized in a recent overview article [14].

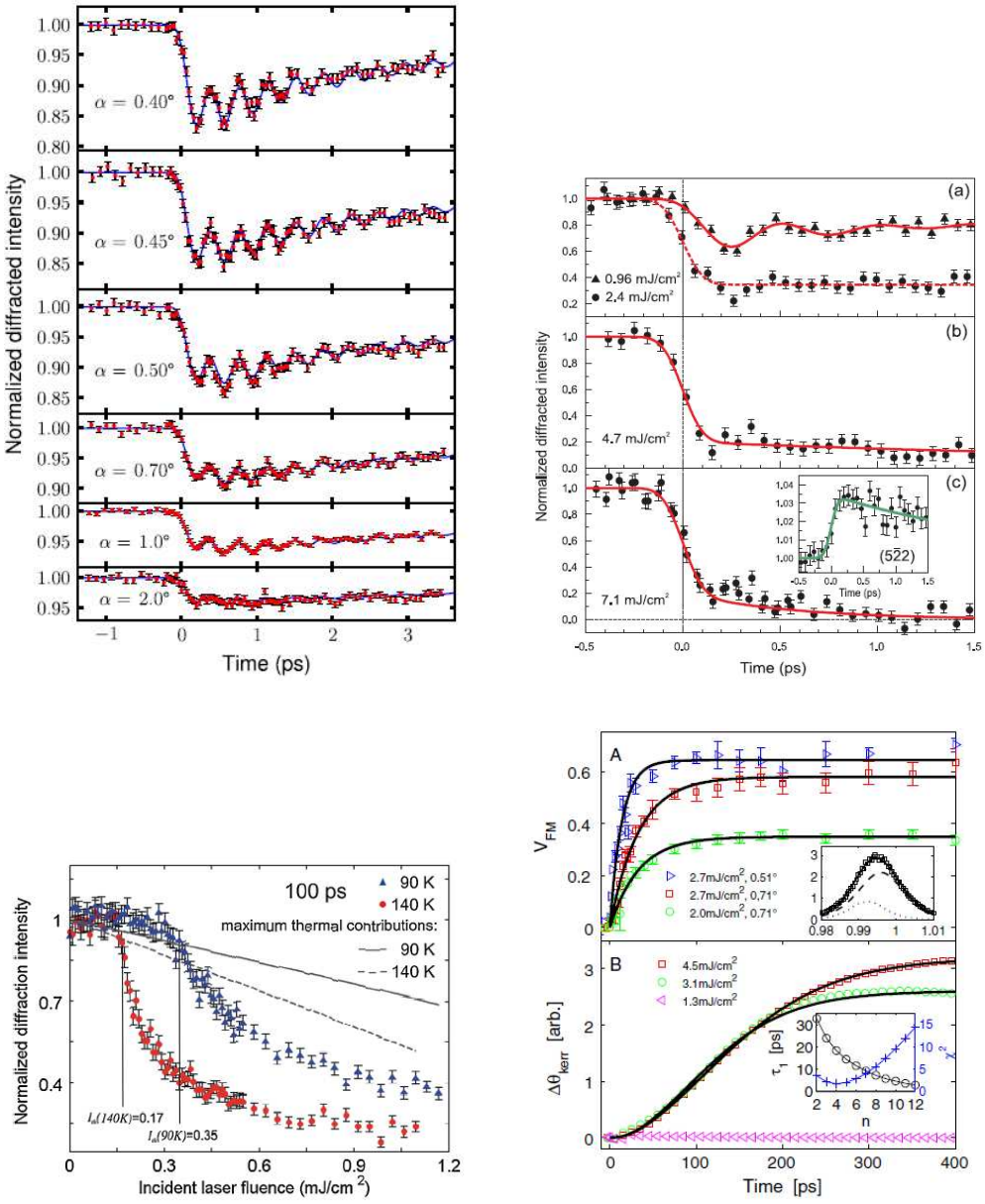

Figure 2.1: **FEMTO highlights: femtosecond structural dynamics.** Top left: Nanoscale depth-resolved and time-resolved diffraction from (111) planes in laser excited bismuth for differentvalues of the grazing-incidence angle α [15]. Top right: Time dependence of the $(5\bar{5}2)$ SL reflection for several pump fluences driven by photoinduced melting of charge and orbital order in LCMO manganite [22]. Bottom left: Nonthermal melting of the excitonic driven CDW in $TiSe_2$. Normalized intensity of the $(\frac{1}{2}, \frac{1}{2}, \frac{1}{2})$ SL peak at 100 ps after excitation. Gray lines correspond to the calculated maximum thermal contribution to the drop in the diffraction intensity [25]. Bottom right: Time dependence of the structural (X-ray diffraction) and magnetic dynamics (MOKE) during the laser induced magneto-structural phase transition in FeRh [26].

2.1.2 Laser induced femtosecond structural dynamics

We propose to use grazing incidence trXRD to approach the question of the electronic or magnetic response of the system in an indirect way by precisely measuring the change of the crystal lattice parameters. This method presumes a strong coupling between the charge-, orbital- and spin states and the lattice. In addition to measuring changes of lattice constants, high-resolution trXRD is sensitive to minute changes in lattice symmetry. To illustrate this, we summarize some of the experiments we have performed in the recent past at the FEMTO slicing source at the SLS [16] employing pump-probe grazing incidence trXRD (some highlight results are shown in Figure 2.1):

- Laser induced coherent acoustic phonon motion and the evolution of strain waves in InSb [17], Bi [14], and carbon-based materials such as graphite [18].
- Large amplitude coherent optical phonon excitation in Peierls distorted semimetals via the displacive excitation mechanism to disentangle the role of electronic transport dynamics (i.e. diffusion of carriers from the surface) from the relaxation of carrier energy via interaction with the lattice in Bi [15], and complete characterization of the unit cell dynamics in comparison with predictions of a density functional theory (DFT) mode in Te [19].
- Directly observing squeezed phonon states [20] and non-fully-symmetric E_g symmetry coherent phonons [21] in bismuth.
- Femtosecond structural dynamics induced by nonthermal melting of charge- and orbital order in Jahn-Teller (JT) distorted perovskite manganites [22, 23, 24].
- Laser induced nonthermal melting of the charge density wave (CDW) in $TiSe_2$ supporting the excitonically-driven model for the transition [25].
- Magneto-structural phase transitions, namely structural and magnetic dynamics of a laser induced paramagnetic (PM)-to-ferromagnetic (FM) phase transition in FeRh [26], and coherent phonon dynamics at the martensitic phase transition in magnetic shape memory (MSM) alloy (MSMA) Ni_2MnGa [27].

2.1.3 Coupled structural dynamics

We discuss the last example in more detail. First, to illustrate that trXRD allows to decompose the evolution of a complex phase transition into subsequent time steps (see Figure 2.2). Nonetheless, complementary X-ray methods are still needed for a full microscopic understanding. Second, it is one example of a broader class of systems where several cooperative phenomena - in this case martensite and ferromagnetism - coexist and interact. There is a great interest for the fundamental understanding regarding the energetics and dynamics of such phenomena [28, 29]. Third, this multiferroic feature (i.e. ferroelasticity and ferromagnetism) is technologically relevant for magneto-mechanical [30, 31] and magneto-caloric [32, 33] applications.

The MSM effect in the Heusler alloy Ni_2MnGa is directly related to a martensitic phase transition. The martensitic transformation (MT) is a diffusionless, solid-to-solid phase transition characterized by a rapid change of crystal structure, accompanied by the development of a rich microstructure. In MSM materials the MT is almost perfectly reversible. Reversibility in this case is solely due to symmetry (i.e. independent of material parameters) and requires that the parent and product phase belong to the same symmetry group. The high temperature (austenite) phase of near-stoichiometric FM Ni_2MnGa is cubic, whereas in the low temperature (martensitic) phase the crystal symmetry is reduced by a tetragonal distortion (and consequently the shape of the material changes due to twinning). In between there exists a premartensitic phase with 5M (or 7M) modulated superlattice (SL) structure (still cubic) stabilized by the band-JT mechanism. The time

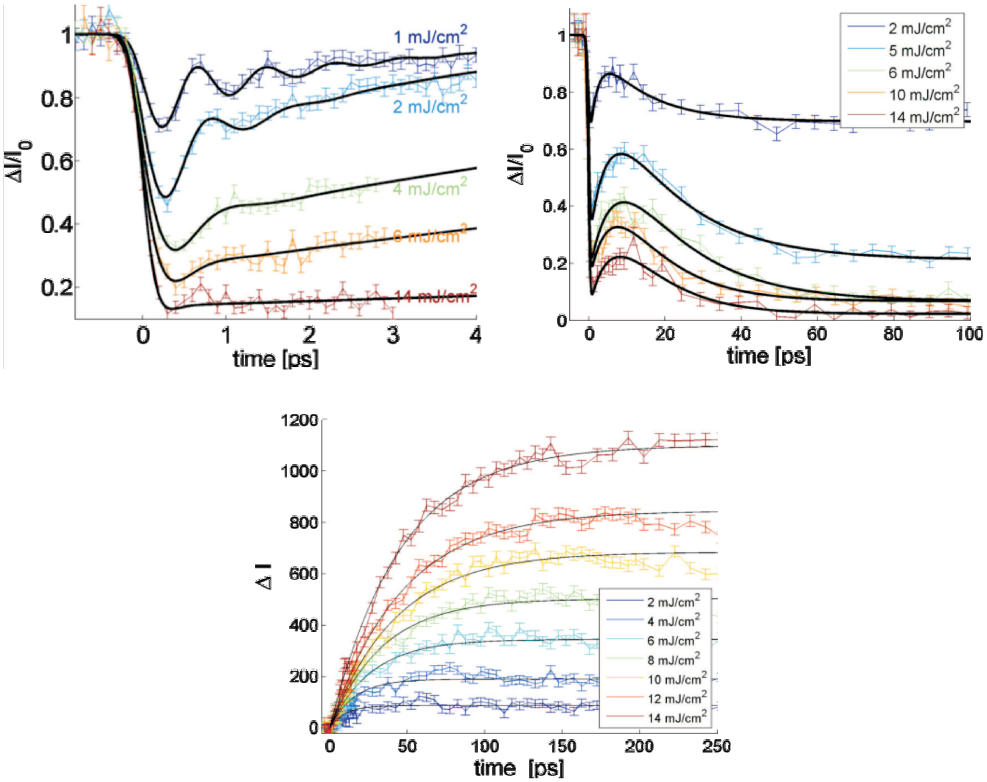

Figure 2.2: **Time resolved hard X-ray diffraction experiment at the FEMTO station at the SLS.** The exeriment was done at 7.05 keV with X-rays under grazing incidence and flux on sample 4 x 10^5 ph/s/1.2% bw using a multilayer-monochromator, X-ray spot size 10 x 200 μm^2 using a set of KB-mirrors, and time resolution 200 fs [34]. The time evolution of the martensitic phase transition in MSMA Ni_2MnGa has been measured, a multi-step magneto-structural phase transition, induced by near-IR (800 nm) laser pulses [27]. The normalized change of the Bragg intensity $\Delta I(t)/I_0$ is plotted as a function of pump-probe delay for various laser fluences. Information about the transient (i.e. change from equilibrium) state during the phase transition is encoded in the functional dependence of I(t) displaying distinctly different time scales and a wide range of dynamical response in the associated structural dynamics. Left panel: Due to JT-relaxation the SL modulation in the 5M modulated premartensitic phase is electronically released on a sup-ps time scale. Center panel: On an intermediate time scale ($\sim$ 5-10 ps) the fast recovery of the modulated SL structure gets suppressed by the thermally induced martensitic transition. Right panel: Time dependence of the tetragonal splitting of the Austenite $[202]_A$ Bragg peak exhibiting 'slow dynamics' due to the rearrangement of twinned domains.

evolution of the transition upon near-IR (800 nm) laser excitation is shown in Figure 2.2 [34].

In the future we plan to extend this study in two ways. First, to perform trXRD measurements in the presence of an external field (1 T) to allow tuning between both phases. Second, to perform (soft X-ray) trXMCD measurements to measure the dynamics of the spin and orbital magnetic moments at the Mn and Ni sites [35, 36]. A direct comparison of the structural and magnetic dynamics [26] should reveal the microscopic mechanism of such a magnetically controlled MT, namely how the twin boundary motion in the modulated phase is coupled to the local magnetic state.

2.1.4 Non-equilibrium phase transitions

Dynamical systems are said to be out-of-equilibrium if the microscopic processes violate detailed balance. Roughly speaking, the term "non- equilibrium" refers to situations where the dynamics is carried by nonvanishing currents (energy, mass, etc.) between microstates and where time is on equal footing with spatial coordiantes [37]. The ability to generate tailored fields of fully coherent light and X-rays opens new possibilities to generate and probe new phases in quantum materials, to understand their properties away from equilibrium, and to direct new excitation paths. Fundamental questions can be addressed in a new way:

▷ *Can XPP experiments contribute to find universality in non-equilibrium phase transitions, and does such universality exist?*

The long term goal would be to achieve an understanding similar to that of equilibrium phase transitions, where the type (universality class) of transition is defined by the symmetry of the order parameter, the range of the interaction, and the dimensionality of space.

▷ *Do fluctuation-dissipation relations exist for systems far from equilibrium ?*

Fluctuation-dissipation relations (FDR) relate the response of a system slightly removed from equilibrium to equilibrium poperties. They allow to connect transport coefficients to microscopic properties [38]. The corresponding quantum derivation was reported in 2008 [39]. In the recent years, there has been growing interest in generalizing FDR to (arbitrarily) far from equilibrium systems. It has been shown that is possible provided the correct conjugate observables are used [40]. To date, no general theory exists capable of predicting macroscopic and fluctuating behaviour in terms of microscopic physics. The consensus is that the study of fluctuations out-of-equilibrium may open the door to such a general theory. The long-term goal is to achieve an understanding similar to that of equilibrium phase transitions, where the type (universality class) of transition is defined by the symmetry of the order parameter, the range of the interaction, and the dimensionality of space.

▷ *What drives non-equilibrium phase transitions ?*

Quantum materials exhibit rich electronic behaviour due to the complex interplay between single-site electron occupation and nearest-neighbour intersite coupling. Upon optical excitation of the single-site occupation, phase transitions can be launched which generally involve abrupt changes in the long-range order of the electronic, magnetic and atomic lattices. The time scale required for this symmetry breaking is determined by an inherently dynamic effect, which should, in principle, limit the speed of such phase transitions, but so far the nature of this limit has not been explored. We have investigated both structural [22, 23, 24] and magnetic [41] order-order phase transitions. We found evidence that a sudden electronic excitation can, in fact, drive a non-equilibrium, order-order phase transition on sub-picosecond time scales, where both the parent and product phases maintain long-range order. Our results indicate that coherent phonon and spin wave excitation, repectively, drive such long-range order-order transitions where the dynamical limit corresponds to the time required for a fraction of an oscillation period. However, a

direct proof is still missing mainly because an order of magnitude better time resolution (30 fs) is needed to resolve the fastest modes.

2.1.5 Quantum critical systems

In a classical second order phase transition the new phase emerges gradually at finite temperature when the system passes a critical point at which interactions with correlations on all length and time scales develop. A quantum phase transition (QPT) occurs at absolute zero temperature (T=0 K) due to a competition between quantum mechanical fluctuations and interactions. It can only be accessed by varying an external parameter. In real systems this may involve the application of hydrostatic pressure P (high pressure cell) or chemical pressure (by doping), changing carrier concentration by chemical doping, and applying a magnetic field H. At finite temperatures the phase diagram (T vs. P or T vs. H) exhibits a quantum critical region (i.e. a region in proximity of the actual QPT transition or quantum critical point) where quantum fluctuations (with energy scale $\hbar\omega$ and classical (thermal) fluctuations (with energy scale k_BT) compete. In this region the quantum system displays scaling relations in space and time (in the same way as classical systems in the vicinity of a continuous phase transition) and quantum and classical effects are interwined and for $\hbar\omega > k_BT$ quantum fluctuations will dominate the systems properties. Stronger fluctuations over a broader range are expected in low-dimensional 1D- and 2D-systems.

Today little is known about the fate of quantum criticality under non-equilibrium conditions. When the system is stimulated with a (large) THz-electric field, it is natural to expect that noise will destroy the subtle correlations underlying the quantum critical behaviour. Interestingly, it has been found that the ubiquitous 1/f noise does preserve the critical correlations and that genuine quantum phase transitions can exist under non-equilibrium conditions [42]. Assuming that a THz-electric field as a non-equilibrium drive does not act as an effective temperature that destroys quantum criticilaty and that different phases retain their integrity, interesting new questions could be addressed:

- Understanding decoherence and relaxation in quantum systems when many-body couplings are involved.
- Evaluating the time scales and range of dynamical response functions (exponential, Gaussian, power-law).
- Evaluating how the dynamics of the system is affected by quantum fluctuations when the change imposed on the system is too fast to be adiabatic.

We propose to study quantum critical behaviour in single crystal materials by applying (selective) vibrational excitation ('phonon pumping') or single cycle high electric field excitation when the system is properly tuned at low temperatures (T$\leq$5 K) and high pressure (P$\simeq$10 GPa) or at high magnetic field (H=12-17 T) according to the phase diagram (T vs. P or T vs. H).

- One class of QPTs would be lattice instabilities where dislocations are locked in place by impurity pinning centers [42] or by a commensurate lattice potential. Crystals with large plasticity and hexagonal crystal structure would be ideal, because large plasticity relies on the presence of many dislocations that can easily move through the crystal and dislocations in hexagonal structures are known to slip easily in the so-called basal plane, which is perpendicular to the long axis (c-axis) of the crystal. However, in classical crystals plasticity is, by definition, irreversible and dislocations can only move by breaking localized bonds [43].
- A second class are pressure-tuned structural superlattice QPTs where the transition temperature of the structural distortion is suppressed with increasing pressure (combining chemical and physical pressure) and extrapolates to T=0 K at a critical

pressure P_c. As an example, the dynamical interplay of a superlattice QPT with superconductivity in a CDW system [44] could be studied.

- A third class are CDW and SDW quantum phase transitions where fluctuations disrupt electron or spin pairing and restore the metallic Fermi surface. This disruption again can be suppressed with applying increasing pressure that the static coherence length of the CDW (SDW) order extends to T=0 K at a critical pressure P_c which can be tracked by measuring the broadening of the CDW (SDW) diffraction line shapes [45]. Another example are low dimensional spin-1/2 AFM systems exhibiting strong spin-lattice coupling [46] to probe stimulated collective spin configurations when the quantum critical magnetic response is tuned with temperature and pressure. The magnetic response is measured indirectly via precise measurement of the crystal lattice parameters or directly employing magnetic trRXRD.

2.2 Time resolved resonant X-ray diffraction (trRXRD)

Regular XPP Bragg diffraction is indirectly sensitive to electronic and magnetic dynamics if there is a strong coupling to the lattice. To overcome this limitation, time-resolved resonant X-rays diffraction (trRXRD) will be employed by combining XPP and RXRD techniques to directly measure the stimulated charge-, orbital- or spin dynamics. RXRD combines the atomic resolution of XRD to probe long-range order with element specific sensitivity of X-ray absorption spectroscopy (XAS) to probe local electronic and magnetic configurations by tuning the X-ray energy to characteristic absorption edges.

A important class of materials to be studied are perovskite oxides of composition ABO_3, where each smaller size (transition metal) B-cation lies at the center of the octahedron defined by the oxydgen anions at the corners, and single layers of larger size (rare earth) A-cations lie between the layers of octahedra. Perovskite oxides are an extremly versatile class of materials, exhibiting a broad spectrum of interesting physical properties, such as

- Superconductivity (in cuprate perovskites)
- Collosal magnetoresistance (in manganite perovskites)
- 2D electron systems at interfaces and interlayer coupling
- Quantum criticality and quantum phase transitions (in bilayer ruthenates and cobalt niobates)
- Metal-to-insulator and charge and spin density wave transitions
- (Anti)ferromagnetism, (anti)ferroelectricity and electromagnons (in pervoskite multiferroics)
- 5d transition metal oxides (spin-orbit driven Mott insulators)

2.2.1 Structural and electronic dynamics

In the following we describe an example which examplifies a whole class of resonant diffraction experiments to clarify the interdependence of structural, electronic and spin order by comparing the time dependence of characteristic structural-, charge-, orbital- and magnetic Bragg reflections.

Earlier we have employed hard X-ray trXRD to observe direct and unambiguous strctural modifications due to laser-induced melting of charge- and orbital-order (CO/OO) phase in a LCMO manganite ([22] and Figure 2.1, top right panel). By measuring the intensity of a Bragg reflection from a superlattice (SL) structural distortion due to the CO/OO state, we were able to study the structural response to strong optical exctiation of the valence electrons. At low excitation fluence insufficient to melt the CO/OO phase, we see the displacive excitation of an approximately 2 THz coherent optical A_g phonon mode that involves motion of the larger size La/Ca cations. When the pump laser fluence is increased to induce the phase transition, we observe quite a different behaviour: a large-scale, sudden drop in the intensity of the SL reflection over a much faster timescale

of < 140 fs. This result indicates that the phase transition involves atomic motion along a structural coordinate different from the coherent phonon observed at lower excitation levels.

To directly address the question how the structural changes are associated with the photoinduced melting of the CO/OO order and in particular how fast the JT-distortion associated with the orbital order is annihilated, we recently have successfully performed non-resonant and resonant pump-probe X-ray diffraction experiments in the vicinity of Mn K-edge (6.55 keV) on PCMO manganite at the XPP instrument at the LCLS (see Figure 2.3 [47]). The Mn K-edge probes the 4p electron band through the 1s-4p virtual transition. Theoretical calculations have shown that the orbital reflection probed at the Mn K-edge is a direct probe of the JT transition [48]. Moreover, hard X-ray XRD can also probe the CO SL reflections [49] which are solely accessible in the hard X-ray regime due to high momentum transfer.

We have measured the intensity of structural peaks, of charge order reflections which occur at $(0, 2k + 1, 0)$ and of orbital order reflections which occur at $(0, k + 1/2, 0)$ (orthorombic notation) [50, 51]. Some of the results are shown in Figure 2.3. The time dependence of the structural reflections provides information about the time which is needed to complete the symmetry change from the Jahn-Teller distorted low temperature to the undistorted high temperature structure. Similarly, the charge and orbital reflections evolve on a timescale where charge and orbital order get suppressed. To find out if this timescale is different from the timescale for the suppression of the Jahn-Teller distortion has been one goal of this experiment.

This example demonstrates that pump-probe tr-RXRS experiments with time resolution better 100 fs are now feasible at XFELs. Although it focuses on the coupling of lattice vibrations with charge and orbital excitations, this method will become much more general by including resonant magnetic scattering and - in addition to time scans - at a fixed time after time zero (pump arrival time) energy- and azimuthal scans, polarization-resolved scans of the diffracted X-rays ($\sigma - \pi$ and $\pi - \pi$ geometry), scans of the resonant scattering intensity versus momentum transfer in reciprocal space, and also the temperature-, pressure- and magnetic field dependence of charge-, orbital- and magnetic ordering intensities.

2.2.2 Manipulating order: selective pump and probe

Phase competition can enable a rapid transformation of a material from an insulator to metal (or superconductor), or from ferromagnet to paramagnet, in response to relatively weak external stimuli. With a far-IR pulse (in the THz-range), low-energy modes can selectively be excited, such as superconducting energy gap, Josephson plasma resonance or specific lattice vibrations. A interesting and new class of experiments are phonon (instead of photon) pumped phase transformations by driving selective structural modes far from equilibrium. All-optical pump-probe experiments using mid-IR and far-IR (THz) pump-pulses have demonstrated

- Vibrational switching of a metal-to-insulator transition by controlling the electronic phase of perovskite manganite via mode-selective vibrational excitation of large-amplitude Mn-O distortions [52];
- Vibrational induced superconductivity by resonantly exciting in-plane Cu-O vibrational modes in a stripe-ordered perovskite cuprate [53].

Another class of experiments are coherent excitations driven by impulsive stimulated Raman scattering which has been demonstrated in an optical-pump / optical-probe experiment:

- Coherent orbital waves in the photo-induced insulator-metal dynamics of a magnetorestive manganite [54].

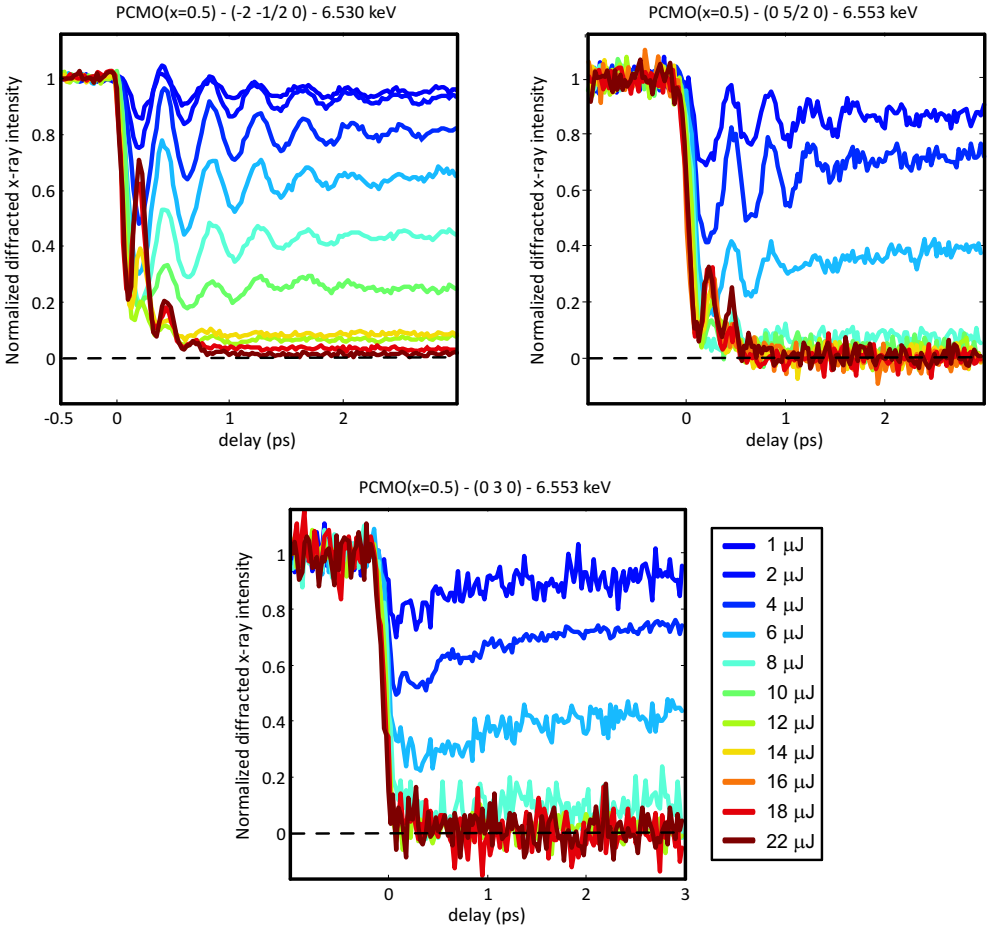

Figure 2.3: **Time-resolved hard X-ray resonant diffraction experiment at the XPP instrument at the LCLS.** The experiment (in April 2013) was done at 6.55 keV with X-ray flux on sample $\sim 10^9$ ph/pulse/0.012% bw using a Si(111) monochromator, X-ray spot size 200 x 200 μm^2 using beryllium refractive lenses, and time resolution better than 100 fs [47]. Non-resonant (structural) and resonant $(0, 2k+1, 0)$ charge- and $(0, k+1/2, 0)$ orbital reflections have been measured at the Mn K-edge of perovskite PCMO manganite after excitation with a near-IR (800 nm) laser pulse at various fluences. Preliminary analysis suggests that the three types of reflections exhibit no difference in timescale but in laser fluence dependence. Whereas the charge- and orbital order melts at fluences above 8 μJ, the structural transition is completed only for fluences above 14 μJ, because motion of the heavier ions to their new equilibrium positions is involved in the structural transition. An interesting new feature is the observation of the reversal of the diffracted intensity when the system is instantaneously driven across the symmetry point ('overshoot'). Since this feature is also present in the charge- and orbital reflections we find that the charge and the Mn-ions do not move independently at times as short as 100 fs. A more careful analysis of all reflections measured will provide information about the direction in which individual atoms have moved during the transition and also will clarify if the strong oscillations observed in the orbital reflection are mainly due to a remnant structural component.

By extending these kind of studies into the X-ray regime, this method will become much more general. In a resonant XPP experiment we not only can selectively excite a particular mode (e.g. a phonon, magnon, or orbiton), but also probe selectively by tuning the X-ray energy to characteristic absorption edges. The result of a tr-RXRD experiment is then direct, mode-specific information how different material excitations interact. For example, resonant excitation of vibrational IR-active modes with tunable THz light ('phonon pumping') and by probing the coupling of the lattice motion to the electronic and magnetic order will allow the precise identification and characterization of these couplings close to thermal equilibrium (i.e. without dumping excess energy into the material as it is often required in optically pumped experiments).

As a first step into this direction we have recently conducted an experiment in the soft X-ray range at the SXR instrument at LCLS that shows that tr-RXRD can probe transient long-range magnetic order by studying the near-IR (800 nm) induced antiferromagnetic phase transition in CuO [41]. A precursor material for the cuprate superconductors, CuO exhibits a AFM collinear-to-spiral phase transition at 213 K. Diffraction with X-rays enegies near the Cu L_3 edge can directly measure the wave-vector of magnetic order across this transition. The ratio of the incommensurate-to-commensurate order begins to change at a few hundred femtosecond delay after laser excitation. Interestingly, the value of this delay depends on laser fluence, and at the highest fluences the value of approximately 400 fs (see Figure 2.4, left panel) is consistent with rough expectations of the minimum time to dynamically reorient the spins across the transition. This limiting time scale corresponds to the time required for a 1/4 oscillation of 1.6 ps spin wave as measured by inelastic neutron scattering. This seems to imply that the first step of the transition is limited by dynamics: the fundamental time required for the long-range magnetic ordering to change. This is analogues to a structural phase transition where the minimum time scale is often expected to be a fraction of phonon period.

2.2.3 Multiferroics: towards field driven switching

Multiferroics (MFs) with coexisting magnetic and electric order are promising functional materials due to the possibility of manipulating the magnetic order (arising from electron spin and associated orbital magnetic moments) by use of electric fields (e.g. without use of resisitive currents) and vice versa. Cross-coupling between two ferroic orders offers possible applications in storage technology and spin based electronics (e.g. spintronics and magnonics). One way to achieve ultrafast switching of the multiferroic state is to coherently excite electromagnons - distinct spin excitations arising from the magnetoelectric coupling - by far-IR THz excitation. Laser based sources of THz frequency radiation can now generate transient electric fields up to 1 MV/cm by optical rectification in crystals[55] or by four-wave mixing in ionized air [56] in the range 0.8 - 3 THz.

As a first step towards this goal we recently performed a tr-RXRD experiment at the SXR instrument at the LCLS where we resonantly excited the highest-energy electromagnon in MF $TbMnO_3$ [57, 58] with a few cycle THz pulse and probed the subsequent spin-spiral motion using soft X-ray resonant magnetic scattering [59]. $TbMnO_3$ belongs to perovskite rare earth manganites, one of the structurally simplest family of MFs, where geometrical distortion due to the incompatibility of the ionic sizes gives rise to variety of spin-frustrated phases. The incommensurate magnetic order of the Mn spins arises on top of the commensurate crystalline structure, forming a spin density wave state below 42 K and a spin-spiral phase below 27 K. For this model compound electrical field induced switching of the helicity of the spin-spiral has been suggested by model calculations [60]. The result shown in Figure 2.4 confirms THz electrical field induced electromagnon excitation and hence the possibility to manipulate the magnetic structure on a subpicosecond time scale. Open questions to be resolved in the future are:

▷ *In which direction and how much do the spins move ?*

▷ *How does the dynamics of the electromagnon affect the quadrupoles or the lattice ?*

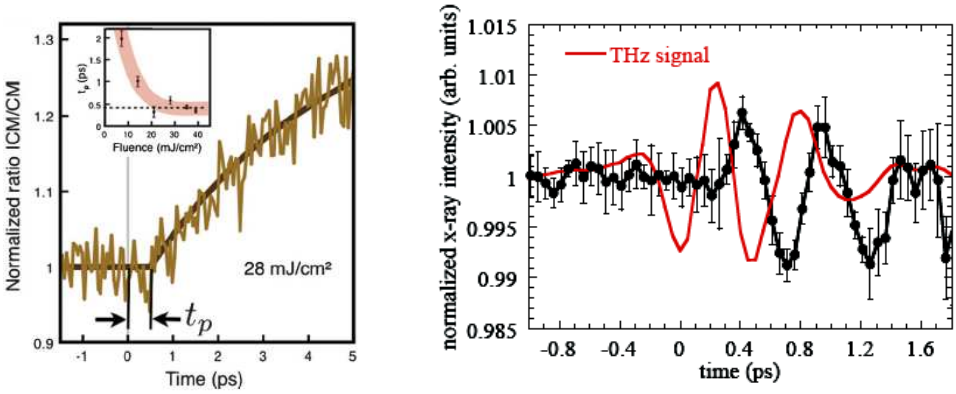

Figure 2.4: **Time-resolved soft X-ray diffraction experiment at the SXR instrument at the LCLS**. Left panel: The experiment was done at 930 eV (near the Cu L_3-edge) with X-ray flux on sample $\sim 10^{10}$ ph/pulse/0.13% bw using a variable-line-spaced plane grating monochromator, X-ray spot size of diameter 300 μm using a set of KB-mirrors, and time resolution 300 fs [41]. The photoexcited dynamics of the collinear/commensurate-to-spiral/incommensurate AFM transition in multiferroic CuO at 207 K (He flow cryostat) has been measured. The relative ICM/CM phase population is shown. The curve is a fit to a delayed biexponential. The insert shows the dependence of the onset time t_p of the phase transition on the excitation fluence. The broad curve drawn here is to guide the eye. The dashed line indicates the time for a 1/4 oscillation of a long-wavelength spin excitation in the CM phase (400 fs). Right panel: Resonant electromagnon excitation in perovskite multiferroic $TbMnO_3$ using a $\sim$ 2 THz electrical field pulse of 350 kV/cm (red curve) [59]. The response is probed by soft X-ray resonant magnetic scattering (0 τ 0) at the Mn L_3-edge (642 eV). The experiment has been performed at the SXR instrument at the LCLS.

2.2.4 Spin-orbit driven 5d transition metal oxides

L-edge resonant scattering in 3d transition metal oxides (TOMs) in the soft X-range have proven to be a powerful technique for the study of electronic and magnetic properties in strongly correlated electron systems, and of high-T_c superconductors in particular. Whereas 3d TOMs have a localized, strongly correlated narrow d-band and large Coulomb repulsion U, 5d TOMs have more weakly correlated wider 5d bands and a smaller U, such that one might expect them to be metallic. However, numerous 5d TOMs, such as iridates and osmates, instead display poor metallic behaviour. Due to the strong spin-orbit coupling (SOC) (400 - 500 meV) that exists in iridates, which is an oder of magnitude stronger compared to the SOC in 3d TOMs ($\leq$ 50 meV), the electronic properties are altered from metallic to a Mott insulator with an exotic magnetic behaviour described by both spin and orbital components. The realization of this novel SOC induced Mott insulating ground and its magnetic structure was first found in perovskite Sr_2IrO_4 using resonant magnetic X-ray scattering at the Ir $L_{2,3}$-edge (11.2 and 12.8 keV) [61] and later in bilayer perovskite $Sr_3Ir_2O_7$ [62]. Later the full magnon dispersion was measured using RIXS [63, 64]. The SOC splits the t_{2g} orbitals into j_{eff}=1/2 (two-fold degenerate) and j_{eff}=3/2 (four-fold degenerate), where j_{eff} denotes the effective total angular momentum derived from the large SOC in the presence of a large crystal field.

As a consequence of the strong SOC the energy scales for magnetic interactions are drastically modified compared to 3d TOMs and surpass that for charge degrees of freedom. Therefore new quantum magnetic effects are expected in 5d TOMs beyond the standard picture of superexchange mediated magnetism for 3d TOMs. Although this field is at its infancy we expect that similar to 3d TOMs time-resolved X-ray scattering will provide new insight into the SOC driven magnetism by directly accessing the dynamics of 5d orbitals by L-edge tr-RSXD and tr-RIXS.

2.3 Time resolved resonant inelastic X-ray scattering (trRIXS)

Resonant inelastic X-ray scattering (RIXS) is a second-order optical process, which involves the electronic dipole transitions, where the incident photon tuned to an absorption edge first excites a core electron to an unoccupied outer valence state accompanied by a quick fill-in of the core hole by an inner valence electron leading to a valence (hole) excitation (intermediate state) that is then replaced by a hole in an outer shell (final state). Interactions of the valence excitations with its surroundings encode information of correlations due to broken symmetries and are seen in the energy loss structure of the RIXS spectra. This way RIXS can excite spin, electronic and lattice modes, with momentum resolution. Hard X-ray K-edge ($1s \rightarrow 4p$) RIXS can measure charge transfer [65, 66], d-d transitions [67] and spin excitations [68, 69] in 3d transition metal systems such as manganites (6.5 keV), nickelates (8.3 keV) and cuprates (8.9 keV). Charge transfer and d-d excitations are accessible with energy resolution 100 - 500 meV and spin excitations with energy resolution 40-100 meV. Recently the polarization dependence, the incident energy dependence, and most crucially, the azimuthal dependence of charge transfer scattering has been used to probe the symmetry of the excitation [70].

Another aspect are X-ray magnetic circular dichroism (XMCD) measurements in combination with hard X-ray ($1s \rightarrow 2p$) RIXS of 3d compounds. The magnetic moments of 3d transition metals are generally studied at the L absorption edge using circularly polarized soft X-rays. It has recently been shown that XMCD combined with RIXS of hard X-rays at the K-edge yields a dichroic signal that is similar in strength to L-edge XMCD [71]. This opens new opportunities to study the dynamics of 3d transition metal magnetic moments and their ordering allowing truly bulk sensitive, element- and site-selective measurements under demanding sample environments.

Hard X-ray L3-edge ($2p_{3/2} \rightarrow 5d$) RIXS probes spin and orbital excitations (as well

as phonons at higher resolution 10-30 meV) in 5d systems such as iridates (11.3 keV) and Os/Re-compounds (10.3-10.9 keV). Most recently the magnon dispersion has been measured in bilayer [64] iridates and the dispersion of an orbital excitation ('spin-orbit exciton') in a single layer iridate [63], a mode that can propagate coherently through the lattice.

Hard L-edge RIXS has several advantages: It has the ability to couple to single magnon excitation (unlike K-edge RIXS), it can access the full Brillouin zone, it is a "direct" process (rather than the "indirect" process of K-edge RIXS) [72], and it profits from reduced matrix element effects [63] (i.e. the momentum transfer may be varied with only relatively small changes in the sample angle meaning that RIXS matrix elements effects are very nearly constant and the intensity dependence arises purely from the dynamic spin susceptibility [73]). Experimentally it requires only compact spectrometers and small samples (unlike neutron scattering), it allows for experiments in complex sample environment (e.g. high pressure), it is not surface sensitive, and non-resonant contributions (Thompson scattering) to the elastic background is largely suppressed for X-rays which are linearly polarized in the scattering plane when data are taken in horizontal geometry with scattering angle close to 90 degrees.

So far no trRIXS experiments have been performed on a fs timescale. By exploiting the high spectral flux in self-seeded operation, trRXRD experiments may be pushed to the inelastic regime by applying time- resolved resonant inelastic X-ray scattering (trRIXS) to measure momentum transfer dispersion of stimulated collective charge and magnetic excitations. Pump-probe RIXS will open a new approach to selectively excite a particular mode (e.g. a magnon, orbiton or phonon) and then observe how this excitation interacts with other modes. Subtle time-dependent features in the dispersion relations and energy line-widths can give information about the higher-order couplings that ultimately lead to electronic correlations. The result is then direct, mode-specific information.

Figure 2.5 (left panel) shows a conceptual example of such an experiment, designed to characterize the coupling of a specific lattice distortion with magnetic interactions [74]. A pump pulse prepares the sample, creating a large amplitude coherent vibration of a particular lattice mode. An appropriately timed X-ray pulse then interrogates the spin wave dispersion in the sample via RIXS, giving direct information on how the vibration couples to spin excitation energies.

We carry this idea a step further and speculate - in case such a system would exhibit quantum criticality - that it may even be possible to measure spin criticality by applying pressure tuning of magnetic fluctuations (by applying hydrostatic and/or chemical pressure). Assuming the system is quasi-two-dimensional and the lattice vibrations are induced by selective 'THz phonon pumping' (i.e. no heat is transferred to the lattice and spin system), antiferromagnetic spin correlations at the QCP develop which should become visible as a broadening of the spin dispersion. Because for a quantum system position and momentum are strictly conjugated, correlations with infinite range in time but localized in space (i.e. localized 'time frozen' magnetic fluctuations) may develop. This is exactly opposite to what happens at the classical critical point where the correlations have infinite range in space but are localized in time (i.e. spatially delocalized waves) [75].

Although the example given above focuses on the coupling of vibrations with spin excitations, this method is much more general. As discussed earlier pump excitations have already been used to trigger charge, spin and orbital excitations [22, 25, 41, 54, 59]. Outstanding questions that time-resolved RIXS can address are (with contributions from [74, 76]):

▷ *How does the magnetic Hamiltonian evolve with time when the system undergoes a non-equilibrium transition ?*

To understand how the melting of magnetic order proceeds; how the ferromagnetic exchange grows at the expense of the antiferromagnetic exchange when a manganite becomes metallic and how this evolution depends on length scale; how the spin excitations evolve in cuprates as superconductivity appears and if they are the same as in the equilibrium

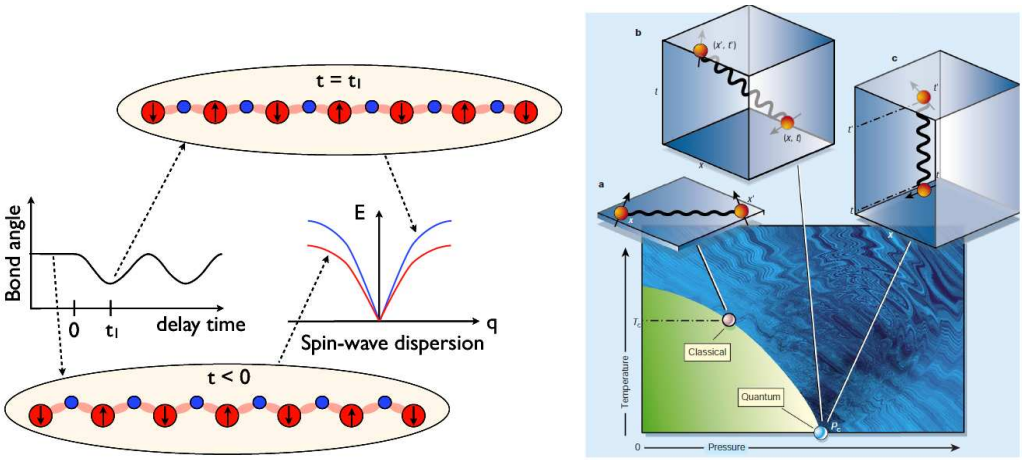

Figure 2.5: **Hypothetical time-resolved RIXS experiment at SwissFEL.** Left panel: A conceptual sketch of the first experiment is shown, a time-resolved RIXS experiment on a hypothetical spin-1/2 Heisenberg antiferromagnet [74]. The pump initiates a coherent lattice vibration at a time = 0 that modulates the angle of the bonds in the antiferromagnet. This causes periodic changes in the energy of spin excitations in the system that can be measured using a short pulse of X-rays to take a "snapshot" of the magnetic interactions. By measuring the spin dispersion at the time t_1 when the lattice distortion is maximized, we gain direct information on the influence of this lattice mode on the effective antiferromagnetic interactions. Right panel: Schematic phase diagram of a magnetic system showing classical (CCP) and quantum critical points (QCP) [75]. This second experiment relates to quantum phase transitions and we speculate that it may be possible to measure spin criticality using trRIXS. Lattice distortions are initiated by selective 'THz phonon pumping' (i.e. no heat transfer to avoid destruction of quantum coherence) to excite spin excitations in a quasi-2D antiferromagnetic spin-1/2 system, similar to the first experiment. In addition we apply pressure tuning of magnetic fluctuations to cause the transition temperature T_c to vanish at the QCP. In the dark blue region above the QCP, electrons may be strongly correlated and no longer move as indipendent particles. At the QCP antiferromagnetic correlations develop which should lead to a broadening of the spin dispersion. At a CCP spin correlations have an infinite range in space, but are localized in time. At a QCP the situation could be different where correlations could have an infinite range in time, but are localized in space (i.e. the exact opposite to what happens at a CCP) [75].

superconductor [76].

▷ *How do electronic correlations arise and what intermediates (phonons, magnons, orbitons, etc.) play an important role ?*

To just give one example, the evolution of orbital excitations as the system goes from insulating to superconducting in the cuprates (a transition not seen in equilibrium) or from antiferromagnetic to ferromagnetic in the manganites [76].

▷ *How does spin dynamics relax in 5d systems ?*

Magnetic RIXS in 5d systems may mark the beginning of a new field. The energy scale of the spin-orbit coupling in 5d elements (several hundred meV) is similar to crystal field energies or the screened Coulomb interaction leading to magnetism which is quite different from the 3d counterparts. To help elucidate the intriguing quantum magnetism in these materials, trRIXS will enable to watch the relaxation of spin- and spin-orbital modes directly. Application of 'phonon pumping' (e.g. selective excitation of bending and stretching modes in the Ir-octahedra [77] will change the relative strengths of the spin-orbit coupling and the non-cubic crystal terms.

▷ *How do the correlations change in response to strong pertubations and can we create far-from-equilbrium transient states even in the non-linear regime ?*

We may ask if it is possible to experimentally turn on and off correlations and if so, on which time scales. The potential ability to experimentally "gate" correlated physics has fascinating potential both in gains to our understanding of exactly how correlations lead to emergent behavior, but also has some technological possibilities. For transient states far-from-equilibrium material properties can in principle be quite different from those encountered under normal laboratory conditions. This opens up the possibility to explore regimes of correlated physics outside the transitional thermodynamic phase diagram, possibly under non-linear conditions. Nonlinear X-ray interactions to probe or even excite coherent excitations are so far difficult to address with current technologies. New X-ray lasers offer an unprecedented level of photon degeneracy (number of photons per electromagnetic mode) that should enable strong nonlinear interactions. These interactions are routinely used in the optical wavelength range to achieve levels of sensitiviy and control over material excitations that are simply not possible with standard linear spectroscopic tools. The question arises if it is possible to extend this into the X-ray range, and if so what are the limitations [74].

▷ *Can we observe quantum criticality under extreme conditions ?*

The classical (renormalization) theory of critical phenomena did not involve any quantum mechanics. Therefore the study of quantum coherence effects over the long distances where critical phenomena play a role is clearly an intriguing prospect. Experiments using X-ray scattering techniques such as tr(N)TDS (which can measure $S(\vec{q}, \omega = 0)$, i.e. the fluctuating coherence length ξ_F) or tr(R)IXS (which can measure $S(\vec{q}, \omega)$, i.e. the full momentum dispersion) under high pressure would be complementary to neutron scattering experiments which study spin criticality at very low temperatures and high magnetic fields using large samples. High pressure requires small samples and therefore a small X-ray spot size. In Figure 2.5 we discuss if selective THz 'phonon pumping' (to avoid destruction of quantum coherence) combined with RIXS could be an avenue to study quantum critical systems with X-rays. This is clearly a speculation, but in any case such a challenging experiment would guide future R&D work that will be needed anyway. If successful, this would open up a new approach to study quantum phase transitions.

Chapter 3

Instrument

The ARAMIS ES-B instrument consists of (1) the femtosecond laser system (pump beam), (2) the X-ray optics (probe beam), (3) the experimental stations for trXRD, trRXRD and trRIXS (including sample environment and detectors), (4) the diagnostic and synchronization systems, and (5) the data acquisition and monitoring system.

There are several groups (optics group, diagnostic group, group for timing and synchronization, laser group, detector group, etc.) which are responsible for the design, construction, installation and operation of subsystems which in total constitute the instrument. Besides the overall design of the instrument, the beamline scientists are responsible for the experimental stations and the operation of the instrument.

Pump-probe experiments in condensed matter at XFELs is a new field that is evolving. As a consequence, proven technology, R& D work and concepts coexist. For this reason - besides the availability of resources - we propose to proceed with the construction of the ES-B instrument in phases. For phase I we consider installations until 2017-2018 and for phase II installations after that ($\geq$ 2018).

3.1 SwissFEL ARAMIS

ARAMIS is the hard X-ray beamline at SwissFEL providing X-rays from a gap variable undulator (in-vacuum, period 15 mm) in the range 0.1(0.08)-0.7 nm at 100 Hz with electron bunches of maximum energy 5.8 (6.5) GeV [1]. The operation with two different bunch charges are foreseen, the *low charge* mode and the *high charge* mode.

For the SASE mode the following X-ray flux and pulse lengths are expected for X-rays of the 1. Harmonic at the end of the undulator (pink beam):

- Low charge mode (10 pC): 7.9 x 10^9 ph/pulse/0.1% bw & 1.8 fs rms
- High charge mode (200 pC): 1.3 x 10^{11} ph/pulse/0.1% bw & 21 fs rms

X-rays of higher Harmonics are also present but much lower in intensity (ratio 3./1. Harmonic $\sim 10^{-2}$, 5./1. Harmonic $\sim 10^{-5}$). ARAMIS will operate both in the SASE and self-seeding mode. For both modes the instrument will be operated with monochromatic and pink beam.

3.2 Femtosecond laser system (pump beam)

For the pump-probe experiments foreseen at ESB the reliable and stable delivery of the *pump pulse* is as important as the stable operation of the accelerator delivering the *x-ray probe pulse*. In addition the synchronization between these sources - or alternatively the accurate knowledge of the time delay between pump and probe pulses - is mandatory to

make optimum use of the ultrashort X-ray pulse duration of a few femtoseconds FWHM offered by the SwissFEL facility.

The wavelength range of interest in solid state physics covers a very broad range (200 nm - 1 mm) starting from electronic transitions typically in the UV/visible/NIR range (0.1 - 5 eV) up to low energy excitations (1-100 meV) such as phonons, magnons, spin or charge-density waves. No single laser system can directly cover such a range, not even a significant fraction of it. However, it is possible to take advantage of the stability and high intensity offered by amplified femtosecond Ti:Sapphire laser systems in conjunction with nonlinear frequency conversion techniques to cover almost the entire frequency range from deep UV up to the THz range. For a particular experiment the pump pulses are derived from the output of a Ti:Sapphire laser system which delivers stable Fourier-transform limited pulses with beams of high spatial quality. This pump laser will be installed in a laser laboratory which is located above the experimental stations. The installation and operation of this laser is not part of the responsibility of the experimental stations.

According to the current planning at SwissFEL the uncompressed output of the pump laser will be transported through a vacuum pipe to an optical table installed next to the experiment. In a first stage the pulses will be compressed and monitored with appropriate diagnostics to optimize the laser properties (pulse width, arrival time and spectra). The optical setup that follows depends strongly on the experiment in question. Routinely we will offer a range of pump energies and pump geometries available to all users. Other more advanced tools may require the close collaboration of the beamline scientists both with the SwissFEL laser and the expert user groups. In the simplest case the 800 nm output pulses can directly be used to excite the sample under investigation. In a more advanced experiment the pump pulses need to be taylored as required by the particular experiment using frequency conversion as well as pulse shaping and compression techniques. In the following we discuss separately the specifications for the laser system and the most important parameters for the excitation pulses needed for the experiments foreseen at ESB.

3.2.1 The pump laser

Since more than two decades *the* laser capable of providing reliable and stable femtosecond pulses is based on Ti:AlO_3 as the laser/amplifier medium and using the chirped pulse amplification technique in combination with diode-pumped Nd-doped pump lasers. Nowadays a typical commercial Ti:Sa laser system reliably delivers stable pulses at $\sim$ 800 nm wavelength, with pulse duration 40 fs and mJ-energies at kHz-repetition rates.

As discussed below some applications will require higher pulse energies. But higher power automatically results in relaxed laser specifications and hence lower performance which we possibly want to avoid. In addition high power operation implies a higher risk of failure due optical damage of optical components in the beam path. For this reason we make in the following a distinction between a *regular laser* system and a *high power option*. The main specifications of the pump laser required to satisfy the experimental needs at ESB are summarized in Table 3.1. Depending on the particular experiment scheduled it should be possible to choose between the regular and high power option.

For efficient use of X-ray beamtime it will be important that the pump laser is always available at the experimental station in order to prepare the next shift/experiment even though one of the other endstations uses the XFEL beam and runs a pump-probe experiment. Therefore a single laser system will not be sufficient to cover the laser needs at all experimental stations. Furthermore, redundancy is needed to avoid a loss of precious and expensive X-ray beamtime in case important laser components have failed.

Regular operation mode	
Pulse duration	30 fs
Pulse energy	3 mJ
Wavelength	800 nm
Repetition rate *	50, 100 Hz
Pulse energy fluctuations	< 1 % rms
Long term power drifts (24h)	< 1 % rms
Pointing stability (24 h)	< 20 μrad
Time bandwidth product	< 1.2
M^2	< 1.2
High power mode	
Pulse duration	< 50 fs (Option: 100 fs)
Pulse energy	20 mJ
Time bandwidth product	< 1.3
M^2	< 1.5

$*$ assuming SwissFEL operated with 100 Hz

Table 3.1: Main pump laser specifications for the regular and high power operation modes, respectively.

3.2.2 Frequency conversion and pulse compression schemes

Electronic excitations: UV-NIR

Typical excitation fluences needed to significantly excite an electronic transition or to induce a phase transition in the material of interest are in the order of one to few tens of mJ/cm^2. Maximum damage thresholds for solid materials are $\sim$200 mJ/cm^2. In fact only a few tens of μJ's focused to a spot size of a few hundred μm is needed to reach such fluences. However 800 nm in almost all cases is not the optimum wavelength to excite the material. It therefore must be possible to convert the wavelength of the pump laser to whatever wavelength needed for the experiment. This can be done by applying nonlinear frequency mixing (or optical parametric amplification) techniques by exploiting materials with high nonlinear optical susceptibilities and the high intensity offered by the Ti:Sa laser. These so called Optical Parametric Amplifiers (OPA's) are quite sophisticated optical systems and are commercially available. With the proposed regular operation mode a laser delivering 40 fs, 2 mJ pulses is sufficient to generate a $> 10\,\mu$J pulse energies ranging from the UV to the mid Infrared.

Selective low energy excitations: farIR-THz

As discussed in section II.2 low energy excitations in the 0.2 - 20 THz frequency range are becoming increasingly important in this area of research. However, the conversion of 800 nm photons to THz photons is difficult and very inefficient and therefore requires the high power pump laser. If possible there should be the option to generate somewhat longer pulses up to $\sim$ 100 fs. The latter would significantly increase the efficiency of the farIR and THz generation [79].

The tuning range that can be obtained with optical parametric amplification techniques can be extended up to a wavelength of $\sim 20\,\mu$m ($\sim$ 15 THz) by increasing the input energy and by adding an additional difference frequency generation stage. Phonon resonances in the nonlinear crystals prevent to further extend this range to even lower frequencies. With a pump energy of $>$ 10 mJ output energies of $> 10\,\mu$J can be generated, up to $\sim 20\,\mu$m (see Fig. 3.1). Phase carrier envelope stable pulses can be obtained by mixing the output of two OPA's sharing the same white light seed [81].

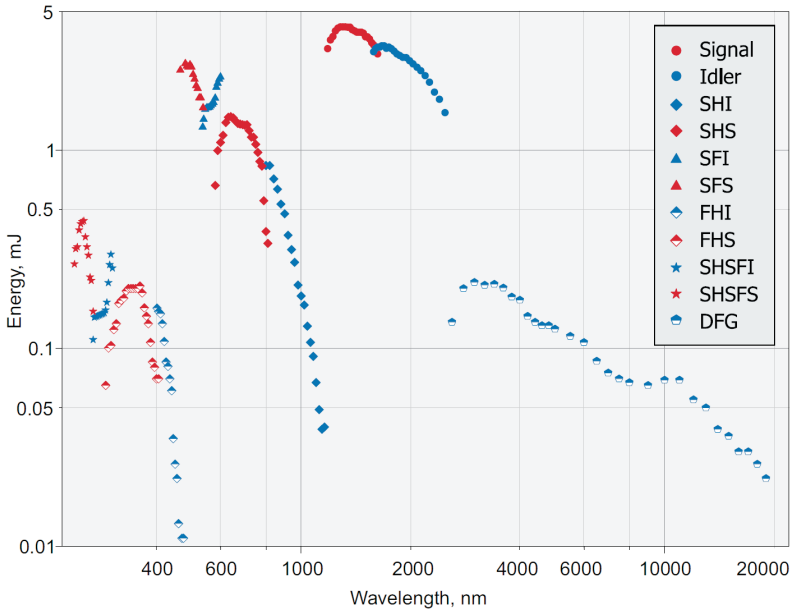

Figure 3.1: Tuning curve of a high energy parametric amplifier (HE-TOPAS-Prime, Light Conversion Inc. [80]). Pump: 22 mJ, 45 fs, 805 nm.

In recent years significant efforts have been made to fill the remaining gap between 0.1 and 15 THz, often called *THz gap*. Using a tilted pump-pulse-front scheme, single-cycle terahertz pulses were generated by optical rectification of femtosecond 800 nm pulses in $LiNbO_3$. In this setup the tilted optical pulse-front requires phase matching of the non-collinear pump- and THz-beams to yield optimal pump-to-THz conversion efficiency [55]. The collimated 0.8 THz beam allows tight focusing with a spot size close to the diffraction limit resulting in a maximum THz electric field of 1.2 MV/cm.

Compared to inorganic crystals such as $LiNbO_3$, organic salt crystals such as DAST provide very large nonlinear optical susceptibilities for optical rectification. When pumped in the $1.2-1.6\,\mu$m spectral range where phase matching between the pump and stimulated radiation is possible, conversion efficiencies of more than 2 % at 2 THz and focused to a field strength of > 1 MV/cm are reported [82]. Recently the SwissFEL laser group in an effort to further extend the frequency range achieved a spectral envelope that contains frequencies up to 5.5 THz [83]. For these applications the high power operation mode together with the high energy OPA is needed to generate the high pump energies required to pump the organic crystals in the NIR frequency range. Despite the recent progress the important gap between 5 - 15 THz still remains. This range covers most of the optical phonon branches in solid materials.

Multicycle vs half-cycle THz pulses

The current developments towards intense THz pulse generation concentrate mostly on the generation of half-cycle pulses providing extremely high electric and magnetic fields at $\sim 1-3$ THz. These very high fields open exciting new applications, for example to control the magnetic phase in multiferroic materials [59]. However, the bandwidth of these half-cycle pulses cover one or several octaves which makes it difficult or even impossible to identify the modes participating in the process. For fundamental research and also for some applications a high selectivity in exciting a specific mode and discrimination of nearby lying modes is of high interest. These applications require the generation of narrower bandwidth multicycle pulses. Using pulse shaping tools the generation of tunable

few cycle pulses in the lower THz range has been demonstrated [84, 85]. However, the challenging task remains to extrapolate these results to higher frequencies, higher fluences and smaller bandwidth.

Pulse compression schemes

SwissFEL will produce X-ray probe pulses with a duration of < 10 fs FWHM. To fully exploit this time scale, pump pulses of similar duration are needed. The compression of the 30 fs down to less than 10 fs can be achieved by taking advantage of spectral broadening of a 800 nm pulse propagating in a hollow-core fused silica fiber filled with atomic and molecular gases. Pulses with duration of < 5 fs have been obtained with pulse energies up to 70 μJ [86]. Commercial devices exists that offer the compression of 30 fs pulses to less than 7 fs with an overall efficiency of 30 % [87]. A big challenge besides the generation of these short pulses will be the appropriate control of the dispersion when propagating such pulses from the source to the sample.

3.2.3 Exciting the sample: pump-probe geometries

Collinear pump-probe geometry

To irradiate the sample with collinear pump and probe beams is the geometry of choice to optimize the time resolution in the experiment. It also is the easiest setup that can be implemented in a complex environment, especially when a vacuum chamber is used. However, there are several constraints to consider:

- For non-grazing incidence angles the probe depth in the hard X-ray range of typically a few μm vastly exceeds the excitation depth of the pump which is typically 10 - 50 nm for opaque materials. This mismatch between the pumped and probed volume dramatically increases the S/B ratio.
- In collinear geometry grazing incidence diffraction is not applicable because the reflection of the pump beam approaches 100 % for incidence angles $< 1°$.
- The combination of collinear geometry and symmetric diffraction is only feasible using miscut samples because the fraction of the laser pump beam reflected from the sample is not allowed to hit the detector or - for safety reasons - the Be or Kapton window in a vacuum chamber.
- At THz frequency a very large numerical aperture of ~ 1 is needed to achieve good focusing conditions (i.e. the focusing mirrors must be brought close to the sample).

For these reasons the collinear pump-probe geometry is only applicable in case of thin films or of materials with low absorption cross sections at the pump wavelength.

Grazing incidence diffraction

This method has to be applied to single crystals of materials where the absorption length of the exciting laser pulse is much smaller than the X-ray probe depth. In this geometry developed at FEMTO [15, 14] the angle between pump and and probe is typically 10 degrees. This geometry has several advantages but also some limitations. The advantages are:

- It can be applied to thin films and crystals.
- Depth dependence by angle tuning yields information on carrier relaxation and diffusion[15].
- For thin films the intensity of the diffracted signal can be increased up to 2 orders of magnitude.

The limitations are:

- The noncollinear geometry leads to an increase of the time resolution. Assuming for example a 5 μm x-ray focus at 0.5° incidence this geometrical contribution to time resolution becomes $\sim$ 30 fs.
- When approaching the critical angle there is a trade off between improving the signal to background ratio and overall diffracted intensity.
- Single crystals with very good surface quality are needed.
- This configuration is not available in the low THz frequency range because of the high divergence of light at these frequencies.

Polarization control by pulse front tilting

In the grazing incidence geometry the pump beam has an incdence angle of $\sim$ 10°. Efficient excitation within the material in this case is only possible for p-polarized light which prevents controlling the polarization of the excitation with respect to the crystal orientation. In this case it is better to pump the sample under normal incidence where the difference in transmission and reflectivity for different polarizations is minimized. To achieve this without deteriorating the time resolution, we can adopte a scheme to tilt the pulse-front of the pump laser by 45° to make the pump-probe delay time nearly constant for normal incidence across the entire pumped region of the crystal [25, 21]. Practically, this is done by imaging the first-order reflection from a grating onto the sample [88].

3.2.4 Summary: pump-probe schemes available at ESB

The following regular pump options and pump-probe geometries should be available for users at ESB from day one:

- Pump wavelength range as offered by regular OPA 400 - 2000 nm.
- Collinear geometry (incidence angle must be larger than $\sim$ 10°): applicable to films and to materials with low absorption cross section at the pump frequency.
- Nearly collinear geometry and grazing incidence diffraction: 10° between pump and probe; applicable to films and crystals; excludes low THz range.
- 10 fs option: 800 nm and collinear geometry only; appropriate pulse diagnostics at the position of the sample might not be available, in particular when using a vacuum chamber.

Other pump wavelengths and application of advanced optical techniques that demand significant efforts to develop or significant changes on the diffractometer setup and/or sample chamber might be possible depending on the man power and laser expertise available at the beamline and the willingness of users to contribute to these efforts. These type of experiments might be:

- Single-cycle THz pulses in the low THz range (depending on the progress made to develop these sources in the near future this might become a regular option).
- Use of extended farIR pump as offered by high power OPA (might become a regular option, once proper diagnostics and expertise is available at the beamline).
- Control of pump pulse shape at arbitrary wavelengths.
- Pump pulse front tilting at arbitrary wavelengths.
- Excitation with carrier phase envelope stabilized farIR pulses.

3.3 X-ray optics (probe beam)

3.3.1 Energy range, monochromatization and tuning

The ES-B instrument uses the 1. Harmonic in the energy range (2.4)4.8-12.4(15.5) keV. For tr(R)XRD experiments a double crystal monochromator (fixed exit, Si(111)/(311)) will be installed (1st mono, installation $<$ 2017). In addition we propose to install a 4-bounce crystal monochromator (Si(400)) (2nd mono, installation $>$ 2018) for tr(R)IXS experiments with resolution 70 - 120 meV, when self-seeding operation of ARAMIS becomes available.

For energy scans the required range is 100-200 eV (1-2% & 12.4 keV). For the SASE mode of operation there are several options to change the X-ray wavelength:

- Monochromator: 0.07 - 0.1% (scanning within FEL bandwidth at higher resolution).
- Broad bandwidth mode: 1 - 4% (but: factor 20-50 intensity loss per bandwidth).
- Undulator gap (K=1.2 - 1.6): 1 - 30% ($\rightarrow$ master/slave undulator/mono scan).
- Electron energy: 100%.

The estimated tuning range in the self-seeding mode is $\sim$ 1%.

3.3.2 Focussing

A focussing mirror system in a Kirkpatrick-Baez (KB) configuration provides achromatic focussing. Two mirrors provide independent focussing (with adaptive bending technology) both in the horizontal (H) and vertical (V) plane. The KB-system is the last optical element installed close to the experimental station. The working distance (i.e. distance between the center of the 2nd mirror and the sample) is 2.5 m. A variable beam spot size at the sample location is required:

- Focal size (HxV) [large/intermediate/small]: 200 x 200 / 10 x 100 / 5 x 5 [μm x μm]

A small spot size in one plane (depending on the sample orientation) is needed for grazing incidence diffraction to minimize geometric pulse lengthening. In addition to high-pressure experiments in a diamond anvil cell, many other experiments benefit if a micro-focus is routinely available.

Refractive beryllium lenses provide chromatic focussing but may be easier to use compared to a KB system. Space should be allocated if possible for later installation of such lenses.

3.3.3 Polarization

Fully variable polarization of the incident X-ray beam in the energy range (3.4)4.8-12.4 keV can be achieved by installing a (single or double) phase retarder (diamond phase plates). Circular and rotated linear polarization can be obtained using quarter-wave plates (QWPs) and half-wave plates (HWPs), respectively. In the hard X-ray regime, QWP and HWP conditions can be obtained by using perfect crystals and slightly detuning them from the ideal Bragg condition [see [89, 90] and references therein].

With such a device *polarization scans* become possible, for instance the generation of incident linearly polarized X-rays at a variable angle η of the linear polarization plane around the beam direction and the analysis of the dependence on η of the Stokes parameters P_1' and P_2' of the diffracted signal from the sample. Polarization scans allow to discriminate between different contributions to the resonant scattering cross section [91]. For magnetic resonant and non-resonant scattering experiments, full polarization scans are used to determine the magnetic moment orientation [92].

We propose to install a UHV double phase-retarder set-up in the optics hutch after the monochromator as an upgrade of the instrument in phase II (> 2018), once it is fully operational. The transmission of the single (double) diamond phase retarder is typically 0.3(0.1). For trRXRD this is acceptable because in our experiments at LCLS in the past the monochromatic beam had to be attenuated typically by a factor 10-20 to avoid sample damage.

3.3.4 Attenuators

A stack of solid state attenuators (> 3 steps per decacade above 6 keV) are used to reach attenuation $> 10^{12}$ for X-ray energies < 15.5 keV. In addition attenuators are designed for 47.5 keV (3. Harmonic of 15.5 keV) to bring the Jungfrau 2D pixel detector into the direct beam.

3.3.5 Slit system

A number of low-Z and high-Z slits with variable horizontal and vertical gap from 0 μm - 10 mm must be available at different locations for shaping the beam and cleaning up parasitic scattering. They must withstand the full X-ray flux (unfocussed) with minimum background scatter from the blades. The last slit system in the beamline will be located in front of the KB system to limit the positional and angular changes to ($\sim 1\mu$m) and ($\sim 1\mu$rad), respectively, which is needed for grazing incidence diffraction.

3.3.6 Harmonic rejection

Radiation above 15.5 keV can be suppressed as follows:

- Pink beam: suppression by the two front-end mirrors (with appropriate coatings) installed in the optics hutch.
- Monochromatic beam with KB-system: suppression by the two mirrors of the KB-system to $< 10^{-4}$. In addition the monochromator can slightly be detuned to reach rejection ratio (3.Harm/1.Harm) $< 10^{-1}$.
- Monochromatic beam without KB-system: in this case the installation of dedicated harmonic rejection mirrors (HRMs) upstream of the KB-system has to be considered in case the experiment is sensitive to higher order contamination.

3.3.7 Windows

A diamond window (thickness: ~ 100 μm, diameter: 10 mm) will separate the beamline vacuum from air. It is mounted inside a vacuum valve which is mounted at the exit port of the KB system. This diamond exit window can withstand the full unfocussed X-ray beam.

3.3.8 Shutter

A fast shutter shall be installed (with sufficient distance) upstream from the diamond exit window to prevent venting of the beamline in case the diamond window is damaged and breaks.

3.4 X-ray diagnostic and synchronization systems

To align and operate the beamline the installation of a range of standard diagnostic tools is required such as beam profile monitors, energy filters, slits, etc. In addition, to take

data with sufficient accuracy using the intrinsically fluctuating SASE FEL pulses, more advanced diagnostic tools must be implemented that can measure shot-to-shot the intensity, the beam position, the relative arrival time between laser and X-ray pulses, and the X-ray photon energy with sufficient accuracy (see Table 3.2. More details of the planned X-ray beam diagnostics at SwissFEL are given elsewhere [93].

3.4.1 Single shot profile monitors

Beam profile monitors (BPMs) with YAG screen allow to optically monitor the X-ray beam using remote zoom and a CCD camera. A resolution of < 10 μm in 2 x 2 mm FOV should be achieved and be capable of a 25 x 25 mm FOV. These devices shall be installed at multiple locations.

3.4.2 Single shot intensity and beam position monitors

Intensity and position monitors (IPMs) shall be installed at multiple locations. These devices are transmissive and measure the Compton backscattering from thin films (thin silicon nitride or diamond targets) to yield the position and intensity on a shot-by-shot basis. The measurement of the intensity I_0 of the incoming X-ray pulses with relative accuracy 10^{-3} is required to determine losses and to normalize the data.

It is important that one of these monitors is installed close to the experimental station after the last slit system (or after any other component that may attenuate or clip the X-ray beam). Monitoring drifts of the beam position will be important in the case of grazing incidence diffraction because a shift in position will cause a shift of the relative timing between the X-ray-probe and the pump.

3.4.3 Single shot spectrometer

In phase I most experiments will use the monochromator. In this case the shot-to-shot measurement of the X-ray wavelength is not needed. For experiments with pink beam a single-shot noninvasive spectrometer would be useful for better binning the data, for example diffuse scattering data [95]. Such a single-shot spectrometer with resolution 2 x 10^{-4} and transmission 95% at 6 keV has recently been demonstrated [96]. In phase II its is planned to install a RIXS spectrometer that uses the seeded SwissFEL beam. For the analysis of the time resolved RIXS spectra the accurate knowledge of the X-ray pulse spectrum may be important for some measurements.

3.4.4 Timing reference distribution

An optical fiber network will be installed by the group responsible for 'timing and synchronization' to distribute a stable timing reference (frequency stability 10^{-10}) for synchronization of critical laser oscillators (gun laser, EO-sampling monitors, pump-laser, etc.):

- Performance goal [jitter & drift/days]: < 10 fs rms & < 10 fs (p-p).
- Potential performance (future) [jitter & drift/days]: < 1 fs rms & few fs (p-p).

3.4.5 XPP timing systems

For X-ray pump-probe experiments two independent timing systems will be installed. The systems will have a different timing accuracy and are designed to be redundant:

- Shot-by-shot electron and laser arrival time measurement: ≤ 50 fs FWHM.
- Shot-by-shot X-ray and laser arrival time measurement: ~ 20 fs FWHM.

The electron bunch arrival time will be measured with a cavity bunch monitor installed at the end of the ARAMIS undulator.

Single shot e-beam/laser time arrival monitors

In a XPP experiment the accurate measurement and control of the relative time arrival shot-by-shot between the pump and the X-ray-probe is crucial for reaching a time resolution set by the respective pulse lengths. The Diagnostic Group at PSI currently develops electron-bunch arrival time (cavity) monitors (BAM) that can measure the electron bunch arrival time relative to a pulsed optical reference with an accuracy of better than 10 fs rms [94]. In addition a laser-pulse arrival time monitor (LAM) will be developed by the laser group to measure the arrival time of the laser pump-pulse (800 nm) at the experimental station with the same accuracy. Even if we allow an additional jitter of the X-ray pulse with respect to the corresponding electron bunch, the combination of BAM and LAM should allow to measure the pump-probe jitter shot-by-shot with an accuracy better than 50 fs FWHM.

Single shot diagnostics required for ES-B experiments	
X-ray pulse intensity	10^{-3}
X-ray position	< 20 μm
Course pump-probe arrival time	< 50 fs
Relative X-ray/laser time arrival	< 20 fs
X-ray pulse width/shape	0.5 fs
X-ray spectrometer *	$< 10^{-5}$

$*$ Not required in phase I, in phase II: for RIXS with seeded FEL

Table 3.2: Specifications of single-shot diagnostic tools needed to perform the proposed pump-probe experiments at ES-B.

Single shot X-ray/laser arrival time

For experiments that require better time resolution a *timing tool* (TT) based on spectral encoding has been developed at LCLS that can measure the jitter between the laser-pump and X-ray-probe with an accuracy of 6 fs rms [97]. We expect to reach 10 fs rms resolution for a timing jitter of 190 fs rms in a time window $\pm$ 1 ps [93].

The advantage of this device is that it requires only a small fraction of the pump laser power and that it can operate in the energy range 5-12 keV. The drawback is that it requires maximum X-ray intensity ($> 10^9$ ph/pulse) in order to give a good timing signal. **The timing tool therefore must be installed upstream of the solid state attenuator**.

For even higher timing precision a *THz-driven streak camera* [98] will be installed that initially will mainly be used for the commissioning of the SwissFEL accelerator. This method can measure the arrival time and pulse length of the X-ray beam with an ultimate accuracy of better than 0.5 fs [93]. For regular diffraction experiments in most cases such an ultimate precision is not needed. However, for potential nonlinear X-ray experiments the accurate knowledge of the X-ray intensity and the temporal pulse shape will be important. Also for the analysis of time-resolved RIXS spectra (proposed for phase II) the accurate knowledge of the temporal and spectral pulse shape may be needed.

3.5 Experimental stations

In Sections 2.1, 2.2 and 2.3 we outlined the scientific case for the trXRD, trRXRD and trRIXS experimental stations. In the following we give a short conceptual overview for

each station in Sections 3.5.1, 3.5.2 and 3.5.3.

3.5.1 trXRD experimental station

This station is similar to the XPP station at the LCLS where we successfully have conducted the experiment described in Figure 2.3, but it will also provide a 2-circle in-vacuum sample rotation stage for trXRD experiments at low temperatures (10 K). This station relies on proven technology and shall be installed in phase I until 2017-2018. It is a general purpose station for a variety of diffraction experiments consisting of a heavy load sample manimpulator, a detector arm and sample environment.

Heavy load sample manipulator

The heavy load (up to 700 kg) manipulator consists of high precision xyz-translation stages, swivel and rotation stages. The stages are commercially available. The manipulator is built in modules and can be reconfigured depending on the needs of the experiment, i.e. the kind of sample rotation stage mounted on top of the manipulator (conceptually this is shown in Appendix B, Figure B.1, top left panel):

- 4-circle sample stage operated in air.
- 2-circle sample stage operated in vacuum.
- Sample goniometer, chamber or other (heavy) equipment provided by the user.

Detector arm and detectors

A large detector arm is needed to position the pixel detector at different angles and distances from the sample with positional accuracy of a fraction of the pixel size. The detector is operated in air (or using He flight tubes). Operation of the pixel detector in vacuum is not considered. Simple translation stages to move the detector as we have used so far will not be sufficient. As installed at XPP/LCLS, a (commercial) robot arm is a much more flexible solution. A big robot can cover a large volume and when mounted at the ceiling does not use valuable floor space. The drawback is that as soon as several installations (vacuum chamber with large exit windows, laser optics, electronic equipment, etc.) are nearby and the motion is not constrained, the pixel detector can hit other sensitve equipment causing severe damage. Although the robot is programmable, we do not plan to operate it in a true diffractometer scanning mode.

The detector will be a 16M Jungfrau 2D pixel detector developed by the PSI detector group. This detector consists of 32 x 0.5M modules with a fixed hole in the center. For experiments where the detector needs to be close to the sample, a single-module 0.5M detector will be used.

Sample environment

Many experiments require variation of the sample temperature (cooling or heating) and the possibility to apply a moderate magnetic field. The following option exists:

- Operation of the 4-circle sample stage in air using LN2 cryojet cooling (min 100 K) and permanent magnet assemblies to apply a magnetic field ($\sim$ 1 T). For THz-pump experiments there is open access to the sample location (see Appendix A, Figure A.1, right panel) which is a tremendous advantage.
- Operation of the 2-circle sample stage in vacuum ($< 10^{-8}$ mbar) with sample temperature 10 - 700 K using a LHe flow cryostat with heating option. In this case a vacuum chamber with a large exit window (beryllium or Kapton) will be used. To avoid frequent bakeout, the chamber will be pumped by installing in addition

LN2 cold traps as cryo-pumps and will use a load station to mount samples under vacuum. In contrast to the chamber we have used so far (see Appendix A, Figure A.1, left panel), all sample stages will be mounted in vacuum to achieve the required roational and translational accuracy of 0.001° and 1 μm, respectively. Such a chamber constraints the type of diffraction experiments that can be done (asymmetric cut crystals, grazing incidence, quasi-collinear laser-pump, etc.) because the exit window for the diffracted X-rays cannot be made arbitrarily large. Therefore space is limited for optics (laser and THz mirrors) and diagnostic tools (EO-sampling, wavefront sensor, etc.) that may have to be mounted inside the chamber.

3.5.2 trRXRD experimental station

What is described here is to a large extent based on the installations at the *Resonant scattering and diffraction beamline P09 at PETRA III* [89]. This beamline covers the energy range 2.7-24 keV and based on proven technology features several state-of-the-art applications which are of high interest for trRXRD experiments at ES-B:

- Small beams and energy tunibility.
- Variable polarization provided by a double-phase retarder.
- A heavy-load diffractometer (in horizontal Psi-geometry) with detector arm that carrys a polarization analyzer stage and can accommodate a variety of sample environments including a 14 T split-pair superconducting (SC) magnet (see Appendix B, Figure B.1, top right panel).
- A high precision 6-circle ('4S+2D') Psi-diffractometer (open χ-circle) with a double detector arm that allows switching from measurements with a point detector (in combination with polarization analyzer stage and beam collimating slits) to measurements with a 2D pixel detector.

Heavy load diffractometer

Because we do not plan to operate the robot detector arm in a true 'diffractometer scanning mode' and mounting a polarization analyzer stage on the robot arm is not feasible, we propose to install a 'reconfigurable heavy load diffractometer' in phase I (until 2017-2018). In its minimum configuration it consists of a reconfigurable heavy load sample stage and a detector arm. Such a device would be similar to the diffractometer shown in Figure B.1 (Appendix B, Figure B.1, top right panel), but without the SC magnet. Reconfigurable means that the diffractometer - depending on the sample environment - can be equipped with a 4-circle sample stage operated in air, with a 2-circle sample stage operated in vacuum, with a SC magnet (see sample environment) or with some other equipment provided by the user.

Polarization analyzer and detectors

On the detector arm a point detector (to measure weak signals) and a 0.5M Jungfrau 2D pixel detector can be mounted at the same time. Although phase retarders may be installed only in phase II ($>$ 2018), the possibility to analyze the polarization state of the scattered X-rays can provide additional information in some experiments. Therefore the point detector should be operated in combination with a polarization analyzer stage.

Sample environment

We distinguish operation with and without high magnetic field:

- No magnetic field: same sample environment as described for trXRD in section 3.5.1.

- High magnetic field: static magnetic fields of several tesla are considered which requires SC magnet technology. Because for time-resolved experiments a standard solution is not available and therefore R&D work will be needed, this mode of operation will only be available in phase II (> 2018).

  Such a project will be in collaboration with the NUM department at PSI that is interested in quantum critical phenomena at high magnetic fields. Conceptually we envision to combine a custom made SC magnet with the vacuum chamber that features the 2-circle sample rotation stage, the LHe flow cryostat for sample cooling, the sample load station, and the large exit window as described for the trXRD station. The SC coil(s) are sealed and fixed inside the vacuum chamber and the sample, attached to a non-magnetic manipulator, is rotated by the 2-circle rotation stage. The magnetic field and sample temperature that can be reached under such conditions is an open question. Recently a (solenoid) 17 T cryomagnet for neutron experiments has been developed with rapid *in situ* sample change and sample temperatures controllable in the range 2 - 300 K [99]. The outer windows are contained in hinged frames, and can be sapphire or silicon, or potentially beryllium or Kapton for X-ray use.

3.5.3 trRIXS experimental station

Time resolved hard X-ray RIXS at XFELs will be a new field and no such experiments have been done so far. Because trRIXS requires high spectral flux, operation of a dedicated station should be considered for phase II (> 2018) when self-seeding of ARAMIS is operational. Prior to the construction of a dedicated station and to gain experience, we propose to operate (in collaboration with experts in this field) a movable RIXS spectrometer arm mounted onto the heavy load sample stage. Such a scenario is shown in Figure B.1 (Appendix B, bottom panel).

What is described here is to a large extent based on the performance of the *MERIX (Medium Energy Resolution Inelastic X-ray Scattering) instrument installed at beamline 30ID at the APS*[100, 76]. This instrument is operated with X-rays in the range 5 - 12 keV (spanning atomic resonances near the K-edge of 3d elements, and the L-edges of 4f and 5d elements) and the micro-focussed flux on sample is 1.2 x 10^{12} ph/s/70 meV at 9 keV.

The X-ray optics is similar to what is proposed for the ES-B instrument and comprises:

- A double crystal monochromator (1st mono, bandwidth $\sim$ 0.6 eV).
- A 4-bounce crystal monochromator (2nd mono, bandwidth 70 meV [with Si(400)] and 120 meV [with Si(220)].
- A focussing KB mirror system to provide micro-focused beams of size $\simeq$ 10 μm x 45 μm.

Compact RIXS spectrometer

The spectrometer arm can be configured from 1 - 2 m. Other relevant features are:

- The polarisation dependence of the scattering at resonance is crucial and is addressed by the ability of the spectrometer to scatter both vertically and horizontally (i.e. polarization selectivity is ensured by vertical and horizontal momentum transfer).
- The analyzer is placed on the spectrometer arm which is set at a scattering angle to define the momentum transfer in Q in the scattering process.
- The spectral resolution depends on the analyzer (for MERIX it varies from $\simeq$ 45 meV to $\simeq$ 170 meV, while the momentum resolution is $\simeq$ 1-4 nm^{-1}.

Crystal analyzer and detector

- The energy analysis of inelastically scattered photons is performed with segmented spherical crystal analyzers in close to Bragg backscattering geometry. For each resonance (edge) a specially designed analyzer is used (for MERIX fabricated from Ge, Si and $LiNbO_3$).
- Since energy dispersion in Bragg diffraction takes place in one plane, a 1D position sensitive detector (PSD) is sufficient.
- The Gotthard micro-strip detector (developed by the PSI detector group) will be used that can provide spatial resolution $\simeq 30$ μm, photon counting mode and quantum efficiency close to 100% for 5 - 12 keV X-rays[101].

Sample environment

Because of the backscattering geometry there is little space between the sample and the micro-strip detector. Cooling samples using a LN2 cryojet in air will be feasible but installation of a vacuum chamber is difficult.

Micro-focussing allows for trRIXS studies at high-pressure (10 GPa) and low temperatures ($<$ 10 K) using a He-loaded diamond anvil cell [102] which requires a small sample size ($\sim$ 70 x 70 x 20 μm^3). THz-pumping (at high P and low T) would also be compatible with such a size (THz radiation can be focussed to a focal size of $\sim$ (2-3) x wavelength, i.e. 10 THz can be focussed to $\simeq$ 50 μm). Depending on the thickness of the diamond window and the X-ray spot size, the highest X-ray energy ARAMIS possibly can reach (15.5 keV) may be needed.

3.6 Data acquisition and monitoring

3.6.1 Data acquisition

Because of the intrinsic fluctuations in the SASE process, the data acquisition system at SwissFEL must be capable - triggered by an event generator - to read out and store shot-by-shot all relevant parameter settings and data readings during an experimental run. This includes data on the characterization and transport of the electron bunch, the laser or THz pump-pulse, the X-ray probe-pulse, the settings of the diffractometer or spectrometer, the parameters on sample environment, and the detector readings at the experimental station. Since this almost always includes the output of one or several (large) 2-D pixel detectors, this typically results in terabytes of data. To limit the data volume, in the case of the large 16M (0.5M x 32 modules) Jungfrau pixel detector data reduction should be applied if possible by defining regions of interest. In the simplest case, a region of interest corresponds to the readout of one 0.5M module.

For time resolved pump-probe studies as foreseen at ES-B it is important to define a sequence of scans where typically one experimental parameter is scanned. For example, in a time delay scan the optical translation-stage for the pump-probe delay is scanned, or simultaneously the sample and detector arm rotation in a $\theta - 2\theta$ diffractometer scan at a fixed time delay. Before a scan is started, it is important to take a snapshot of all those parameters and settings of the beamline and the experimental station that are relevant for the experiment but do not change during a scan and therefore do not have to be stored shot-by-shot.

3.6.2 Data monitoring

Fast access to the measured data for analysis during the experiment will be crucial. This implies fast data transfer and efficient data analysis of large data sets to minimize the time needed to analyze a scan before the next one is started. During the experiment the

goal is to extract sufficient information from previous scans to decide on the next step in a sequence of scans in order to optimize the procedures (parameter settings, scan range, etc.) during the experiment and finally to take a complete set of data. Missing information may lead to an incomplete data set. Therefore the delay between data acquisition and preliminary data analysis must be kept to a minimum. The more shot-to-shot corrections to the data are needed to see an incremental improvement during optimization of the experiment, the more time for data analysis will be needed.

Therefore efficient online data reduction tools will be needed to reduce the data such that online monitoring of an ongoing scan is feasible with sufficient accuracy. The most important online corrections are the shot-by-shot intensity normalization and the rebinning of the data by applying timing jitter corrections. Whereas for data monitoring only a subset of the data will be analyzed, the complete data set is stored for analysis once the experiment is done.

Acknowledgement

The authors of this paper are greatful for many fruitful discussions.

FEMTO group: A. Caviezel, A. Ferrer, S. Grübel, J. Johnson, A. Lübcke, S. Mariager;

SwissFEL project: R. Abela, Ch. Hauri, P. Juranic, C. Milne, A. Mozzanica, B. Pedrini, L. Patthey, B. Patterson, L. Sala;

SYN department: U. Flechsig, R. Follath, B. Schmitt, Th. Schmitt, U. Staub, P. Willmott;

NUM department: M. Barthowiak, M. Kenzelmann;

GFA department: S. Hunziker, S. Reiche, V. Schlott;

ETH Zuerich: S. Johnson, T. Huber;

BNL: J. Hill;

CFEL: M. Först;

DESY: J. Strempfer;

LCLS: R. Coffee; D. Fritz; R. Lembke; M. Trigo;

Bibliography

[1] http://www.psi.ch/swissfel.

[2] F. Schmitt et al., Science 321 (2008) 1649.

[3] T. Rohwder et al., Nature 471 (2011) 490.

[4] C. Kübler et al., Phys. Rev. Lett. 99 (2007) 116401.

[5] M. Eichberger et al., Nature 468 (2010) 799.

[6] S. W. Lovesey and S.P. Collins, *X-ray Scattering and Absorption by Magnetic Materials*, Clarendon Press, Oxford, 1996.

[7] S. Sachdev, *Quantum Phase Transition*, Cambridge University Press, Second Edition, 2011.

[8] Ch. Bressler et al., Science 323 (2009) 489.

[9] M. Chollet et al., Science 307 (2005) 86.

[10] E. Collet, Acta Crystallogr. A 66 (2010) 133.

[11] F. Zamponi et al., PNAS 109 (2012) 5207.

[12] J.N. Clarke et al., Science Express (2013) DOI.10.1126/science.1236034.

[13] M. Först et al., Nature Physics 7 (2011) 854.

[14] S.L. Johnson et al., Acta Cryst A 66 (2010) 157.

[15] S.L. Johnson et al., Phys. Rev. Lett. 100 (2008) 155501.

[16] P. Beaud et al., Phys. Rev. Lett. 99 (2007) 174801.

[17] F.S. Krasniqi et al., Phys. Rev. B 78 (2008) 174302.

[18] M. Harb et al., Phys. Rev. B 84 (2011) 045435.

[19] S.L. Johnson et al., Phys. Rev. Lett. 103 (2009) 205501.

[20] S.L. Johnson et al., Phys. Rev. Lett. 102 (2009) 175503.

[21] S.L. Johnson et al., Phys. Rev. B 87 (2013) 054301.

[22] P. Beaud et al., Phys. Rev. Lett. 103 (2009) 155702.

[23] A. Caviezel et al., Phys. Rev. B 86 (2012) 174105.

[24] A. Caviezel et al., Phys. Rev. B 87 (2013) 205104.

[25] E. Möhr-Vorobeva et al., Phys. Rev. Lett. 107 (2011) 036403.

[26] S.O. Mariager et al., Phys. Rev. Lett. 108 (2012) 087201.

[27] S.O. Mariager et al., Appl. Phys. Lett. 100 (2012) 261911.

[28] K. Bhattacharya et al., Nature 428 (2004) 55.

[29] V.D. Buchelnikov et al., Phys. Rev. B 81 (2010) 094411.

[30] J. Cui et al., Nat. Mater. 5 (2006) 286.

[31] I. Takeuchi et al., Nat. Mater. (2003) 180.

[32] T. Krenke et al., Nat. Mater. 4 (2005) 450.
[33] J. Liu et al., Nat. Mater. 11 (2012) 620.
[34] S.O. Mariager, to be published.
[35] C. Stamm et al., Nat. Mater. 6 (2007) 740.
[36] I. Radu et al., Nature 472 (2011) 205.
[37] M. Henkel, H. Hinchrichsen, S. Lübeck, Non-Equilibrium Phase Transitions, Springer, 2008.
[38] R. Kubo, Rep. Prog. Phys. 29 (1966) 255.
[39] D. Andrieux and P. Gaspard, Phys. Rev. Lett. 100 (2008) 230404.
[40] J. Prost et al., Phys. Rev. Lett. 108 (2012) 037203.
[41] S.L. Johnson et al., Phys. Rev. Lett. 108 (2012) 037203.
[42] E.G. Dalla Torre et al., Nat. Physics 6 (2010) 806.
[43] B. Castaing, *Plastic Quantum Crystals*, Physics 6, 5 (2013).
[44] L.E. Klintberg et al., Phys. Rev. Lett. 109 (2012) 237008.
[45] Y. Feng et al., PNAS 109 (2012) 7224.
[46] S. Haraviford et al., PNAS 109 (2012) 2286.
[47] A. Caviezel et al., to be published.
[48] M. Benfatto et al., Phys. Rev. Lett. 83 (1999) 636.
[49] S. Grenier et al., Phys. Rev. B 69 (2004) 134419.
[50] M. v. Zimmermann et al., Phys. Rev. Lett. 83 (1999) 4872.
[51] M. v. Zimmermann et al., Phys. Rev. B 64 (2001) 195133.
[52] M. Rini et al., Nature 449 (2007) 72.
[53] D. Fausti et al., Science 331 (2011) 189.
[54] D. Polli et al., Nat. Mater. 6 (2007) 643.
[55] H. Hirori et al., Appl. Phys. Lett. 98 (2011) 091106.
[56] T. Bartel et al., Opt. Lett. 30 (2005) 2805.
[57] T. Kimura et al., Nature 426 (2003) 55.
[58] Y. Takahashi et al., Phys. Rev. Lett. 101 (2008) 187201.
[59] T. Kubacka et al., to be published.
[60] M. Mochizuki et al., Phys. Rev. Lett. 105 (2010) 147202.
[61] B.J. Kim et al., Science 323 (2009) 1329.
[62] J.W. Kim et al., Phys. Rev. Lett. 109 (2012) 037204.
[63] J. Kim et al., Phys. Rev. Lett. 108 (2012) 177003.
[64] J. Kim et al., Phys. Rev. Lett. 109 (2012) 157402.
[65] J. Hill et al., Phys. Rev. Lett. 80 (1998) 4967.
[66] Y.-J. Kim et al., Phys. Rev. Lett. 92 (2004) 137402.
[67] K. Ishii et al., Phys. Rev. B 83 (2011) 241101.
[68] J. Hill et al., Phys. Rev. Lett. 100 (2008) 097001.
[69] D.S. Ellis et al., Phys. Rev. B 81 (2010) 085124.
[70] G. Chabot-Couture et al., Phys. Rev. B 82 (2010) 035113.
[71] M. Sikora et al., Phys. Rev. Lett. 105 (2010) 037202.

[72] L.J.P. Ament et al., Rev. Mod. Phys. 83 (2011) 705.

[73] L.J.P. Ament et al., Phys. Rev. B 84 (2011) 020403(R).

[74] S.L. Johnson, private communication (2013).

[75] P. Coleman, Nature 413 (2001) 788.

[76] J. Hill, seminar at PSI (2012), and private communication (2013).

[77] S.J. Moon et al., Phys. Rev. B 80 (2009) 195110.

[78] J. Johnson, S. Grübel et al., to be published.

[79] M. Först, MPSD/CFEL, private communication (2013).

[80] http://www.lightcon.com/

[81] C. Manzoni, M. Frst et al., Opt. Lett. 35 (2010) 757.

[82] C. P. Hauri, C. Ruchert, C. Vicario, and F. Ardana, Appl. Phys. Lett. 99 (2011) 161116.

[83] C. Ruchert, C. Vicario, and C. P. Hauri, PRL 110 (2013) 123902.

[84] T. Feurer et al. Opt. Lett. 29 (2004) 1802.

[85] Z. Chen et al., Appl. Phys. Lett. 99 (2011) 071102.

[86] M. Nisoli et al., Appl. Phys. B 65 (1997) 189.

[87] http://www.femtolasers.com/

[88] J. Hebling, Opt. Quantum Electron. 28 (1996) 1759.

[89] J. Strempfer et al., J. Synchrotron Rad. 20 (2013) 541.

[90] S. Francoual et al., SRI 2012, J. Phys.: Conf. Ser. 425 (2013).

[91] C. Mazzoli et al., Phys. Rev. B 76 (2007) 195118.

[92] R.D. Johnson et al., Phys. Rev. B 78 (2008) 104407.

[93] Pavel Juranics, SwissFEL Photon Beam Diagnostics (CDR), Draft (2013).

[94] Stephan Hunziker, GFA, Paul Scherrer Institut, private communication (2013).

[95] M. Trigo et al., arXiv:1301.3503v1 (2013).

[96] P. Karvinen et al., Opt. Lett. 37 (2012) 5073.

[97] M. Harmand et al., Nature Photonics 7 (2013) 215.

[98] U. Fruehling et al., Nature Photon. 3 (2009) 215.

[99] A.T. Holmes et al., Rev. Sci. Instrum. 83 (2012) 023904.

[100] Yu.V. Shvyd'ko et al., J. Electron. Spectrosc. Relat. Phenom. (2012), http://dx.doi.org/10.1016/ j.elspec.2012.09.003.

[101] B. Schmitt, PSI detector group, private communication (2013).

[102] Y. Feng et al., Rev. Sci. Instrum. 81 (2010) 041301.

Appendix A

R&D work at FEMTO

Figure A.1. Upper panel: Low temperature (35-300 K) XPP vacuum chamber (5 x 10^{-8} mbar with turbo pump and LN2 cold trap) for laser-pump / X-ray-probe grazing incidence diffraction experiments installed at FEMTO. The pixel detector (2D Pilatus) is mounted in air. The chamber uses an out-vacuum hexapod sample manipulator with ϕ-rotation for sample alignment and rotation, a closed-loop cryocooler for cooling the sample, and a large exit window (single layer aluminized Kapton, thickness 20+125 μm) to pass the diffracted X-rays. At ARAMIS ES-B we also plan to operate the pixel detector (16M 2D Jungfrau) in air. The XPP chamber will be a UHV cryo chamber with the following improvements: differentially pumped double-layer Kapton-window or beryllium-window (vacuum $<$ 8 x 10^{-9} mbar), He-flow-cryostat with heating option (sample temperature 10-700 K), and 2-circle in-vacuum goniometer (angular accuracy 0.001° and positional accuracy 1 μm).

Lower panel: Experimental setup used for a THz-pump / X-ray-probe diffraction experiment at the new FEMTO station in April 2013 which consists of an in-vacuum multilayer monchromator and a large acceptance KB mirror system. Single cycle THz-pulses at $\sim$1 THz and E$\sim$280 kV/cm are generated via optical rectification in an organic crystal (OH_1) with high nonlinear optical coefficient pumped with 250μJ at 1350 nm using an OPA. The OPA is pumped with a Ti:Sapphire regenerative amplifier (800 nm, 150 fs, 1.4 mJ, 1 kHz). A combination of two parabolic mirrors is used for the THz-focussing. For in-situ characterization and alignment an electro-optical crystal is mounted next to the sample [78].

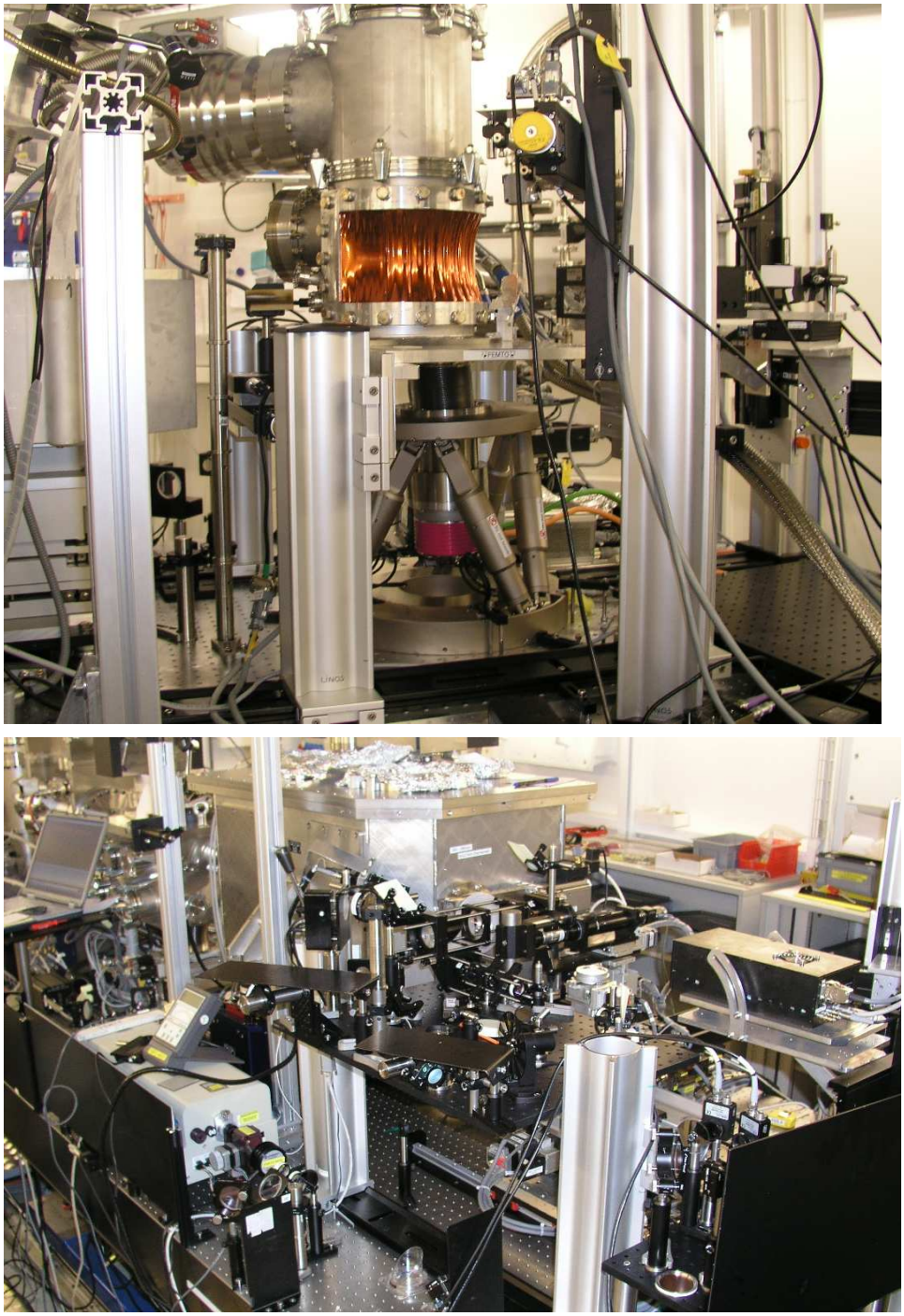

Figure A.1: **Present R&D work relevant for the ARAMIS ES-B instrument: XPP vacuum chamber and THz-pumping.**

Appendix B

Experimental stations proposed

Figure B.1: Top left panel: General purpose heavy load sample manipulator for trXRD experiments (equipped with XPP UVH cryo chamber (T = 10-700 K)).

Top right panel: Heavy load diffractometer for trRXRD experiments (with polarization analyzer mounted on the detector arm and equipped with a superconducting (SC) magnet, B = 10-14(17) T) [courtesy: J. Strempfer (DESY) and S. Griessel (Huber GmbH)]

Bottom panel: Compact RIXS spectrometer arm for trRIXS experiments (equipped with a diced crystal analyzer, 1D Gotthard strip detector and high pressure cell (not shown); installation prior to construction of a dedicated trRIXS-spectrometer) [spectrometer arm design: S. Coburn, B. Leonhardt and J. Hill (BNL)].

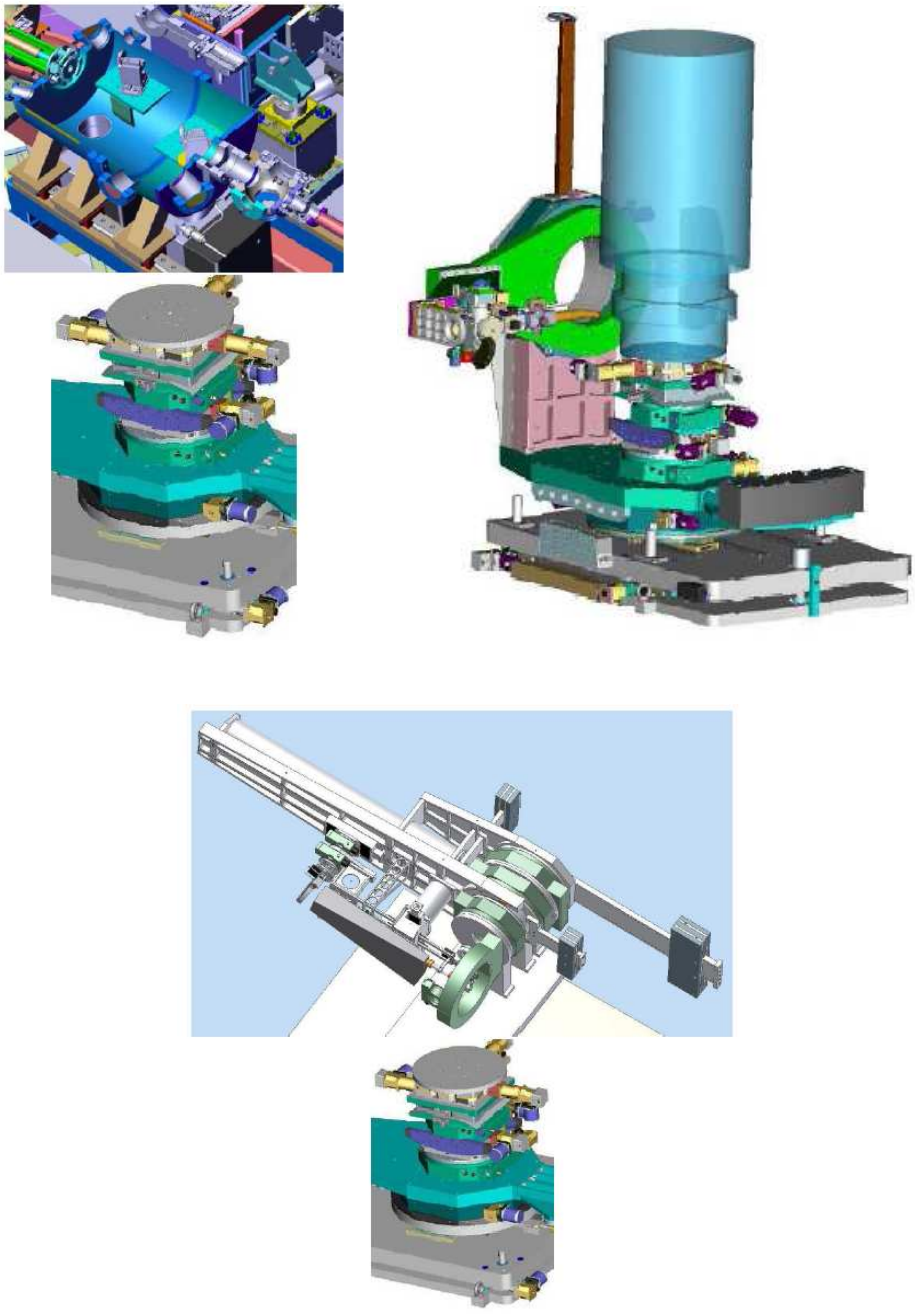

Figure B.1: **Proposed experimental stations for SwissFEL ARAMIS ES-B:**